

Exciton Proliferation and Fate of the Topological Mott Insulator in a Twisted Bilayer Graphene Lattice Model

Xiyue Lin,^{1,2} Bin-Bin Chen,^{3,4,*} Wei Li,^{1,4} Zi Yang Meng,^{3,†} and Tao Shi^{1,‡}

¹CAS Key Laboratory of Theoretical Physics, Institute of Theoretical Physics, Chinese Academy of Sciences, Beijing 100190, China

²School of Physical Sciences, University of Chinese Academy of Sciences, Beijing 100049, China

³Department of Physics and HKU-UCAS Joint Institute of Theoretical and Computational Physics,

The University of Hong Kong, Pokfulam Road, Hong Kong, China

⁴School of Physics, Beihang University, Beijing 100191, China

(Dated: May 26, 2022)

Topological Mott insulator (TMI) with spontaneous time-reversal symmetry breaking and nonzero Chern number has been discovered in a real-space effective model for twisted bilayer graphene (TBG) at 3/4 filling in the strong coupling limit [1]. However, the finite temperature properties of such a TMI state remain illusive. In this work, employing the state-of-the-art thermal tensor network and the perturbative field-theoretical approaches, we obtain the finite- T phase diagram and the dynamical properties of the TBG model. The phase diagram includes the quantum anomalous Hall and charge density wave phases at low T , and a Ising transition separating them from the high- T symmetric phases. Due to the proliferation of excitons – particle-hole bound states – the transitions take place at a significantly reduced temperature than the mean-field estimation. The exciton phase is accompanied with distinctive experimental signatures in such as charge compressibilities and optical conductivities close to the transition. Our work explains the smearing of the many-electron state topology by proliferating excitons and opens the avenue for controlled many-body investigations on finite-temperature states in the TBG and other quantum moiré systems.

Introduction.— Since the discovery of correlated insulators and superconducting states in the magic-angle twisted bilayer graphene (TBG) [2, 3], the quantum moiré systems [4–6] become an active playground for experimental and theoretical investigations on exotic phenomena [7–36]. The intriguing quantum effects in TBG and transition metal dichalcogenide (TMD), besides the superconductivity, encompass a wide range including the orbital ferromagnetism [9, 15], (emergent) quantum anomalous Hall (QAH) effect [15, 16, 34, 37, 38], large (iso)spin entropy and Pomeranchuk effect [19, 20], etc. Such a plethora of quantum states is believed to originate from the interplay of strong electron correlation and fragile band topology [39–53]. Many theoretical models have been put forward to address these interesting phenomena, and among the positive semidefinite Hamiltonians that are proposed [46, 50, 54, 55], a real-space effective model by Kang and Vafeek (KV) is able to integrate both key ingredients [54, 56]. The KV model and its variants have been investigated via quantum Monte Carlo simulations, which showed certain correlated insulating states such as the inter-valley coherent and quantum valley Hall states, etc, are natural ground states at integer fillings and particularly the charge neutral point (CNP) of the TBG systems [57–60].

Away from CNP, density matrix renormalization group (DMRG) simulations upon the KV model revealed that a QAH state can emerge purely from interactions at 3/4 filling [1], which constitutes the long-sought-after topological Mott insulator (TMI) [61]. Along with other scenarios [47, 51, 62] that give rise to the Chern insulators at odd fillings, such a *bona fide* TMI state provides a strong coupling explanation of the observed quantized Hall conductance in experiments [15, 16]. Although the ground state with non-trivial topology in the TBG model is known, the low-energy collec-

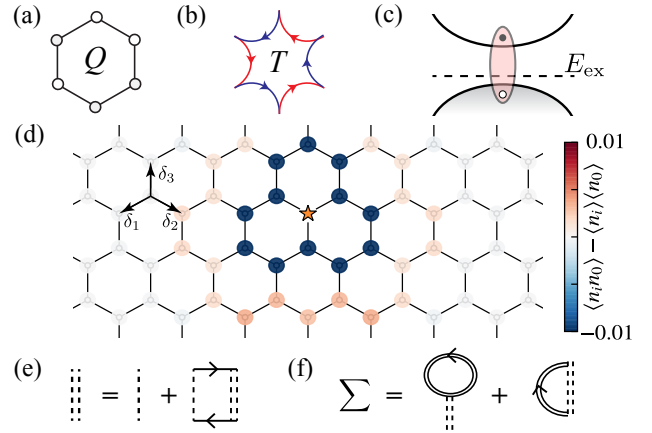


FIG. 1. The KV model with (a) the cluster charge Q and (b) assisted hopping T terms. (c) illustrates the formation of exciton between two quasi-particles from the valence and conduction bands. (d) shows the charge correlations between a central site (the asterisk) and other sites, at intermediate temperature $T = 0.244$ inside the exciton proliferation regime. The vectors δ_i are introduced to display the charge correlations in Fig. 3(d). (e) shows the scattering T -matrix that is the renormalized interaction of electrons by the contributions of the ladder diagrams. (f) shows the Hartree-Fock-like contribution to the self-energy of the single-particle Green's function.

tive excitations and the experimentally relevant finite- T phase diagram are still absent. As the QAH state spontaneously breaks time reversal symmetry (TRS), a thermal phase transition is expected to take place between the topological QAH and high- T symmetric phase. However, a naive estimate of the transition temperature T_c according to the band gap [1] — based on the mean field theory — leads to a value of the order of 100 K, higher than the experimental value ($\lesssim 10$ K) by an

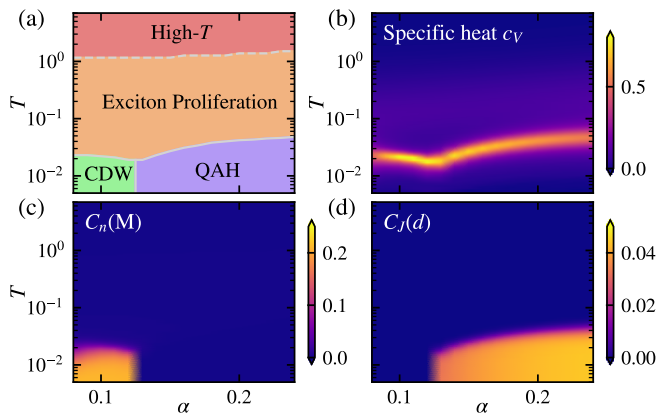


FIG. 2. (a) Finite-temperature phase diagram of the KV model, with the red regime being the high- T disorder phase, the intermediate- T orange one where exciton proliferates, the green one being the CDW phase, and the purple one being the QAH phase. The phase transition line between the low- T symmetry breaking and the symmetric phase at intermediate T , as well as the crossover temperatures (white dashed line) between intermediate- to the high- T regimes are determined from analyzing the specific heat c_V data. Supporting the phase diagram in panel (a), we map the α - T landscapes of (b) specific heat c_V , (c) charge structure factor $C_n(M)$, and (d) current correlation $C_J(d)$ at a distance of $d = 6$ to clearly identify the phase boundaries.

order of magnitude [9, 15]. The difference is believed to stem from the intertwinement of electronic interaction and thermal fluctuations.

To elucidate the thermal melting of the topological phase and the associated phase diagram, we perform accurate finite- T many-body calculations with the exponential tensor renormalization group (XTRG) method [63, 64]. XTRG calculations uncover an Ising-type thermal phase transition between the low- T QAH phase and the symmetric phase, and a critical temperature reduced by one order of magnitude compared to the mean-field estimation. These observations are further explained by a field-theoretical approach, which unveiled the emergence of a collective mode of a bounded particle-hole pair–exciton. The excitons are found to have a rather flat and low lying dispersion and proliferate as the temperature elevates, playing an essential role in the melting of the low- T phase. The proliferation of excitons leads to a modulation of electron-hole correlations in real space. The entire finite- T phase diagram including the low- T QAH and CDW phases and the intermediate exciton proliferation phase, is accurately mapped out via both XTRG and field-theoretical approaches.

These results extend the understanding of the zero-temperature phase diagram to finite-temperature and dynamical effects of collective excitations [32, 65], beyond the exactly solvable limits [51, 52, 54, 65–67]. Distinctive signatures of the exciton proliferation phase are also revealed to bridge the experimentally accessible observables with theoretical understanding.

Real-space TBG model, thermal tensor networks, and field-theoretical approach.— The KV model considered here is de-

scribed by the interaction-only Hamiltonian

$$H = U_0 \sum_{\square} (Q_{\square} + \alpha T_{\square} - 1)^2, \quad (1)$$

where $U_0 = 1$ sets the energy unit (~ 40 meV in realistic system [1]), the cluster charge term $Q_{\square} \equiv \frac{1}{3} \sum_{l \in \square} c_l^{\dagger} c_l$ counts the numbers of electrons in each hexagon [c.f., Fig. 1(a)], and $T_{\square} \equiv \sum_{l \in \square} [(-1)^l c_l^{\dagger} c_{l+1} + \text{h.c.}]$ represents the assisted hopping term with alternating sign [c.f. Fig. 1(b)]. The results of the present work are mainly based on the $YC4 \times L$ geometry with $L = 12$, where the lattice is under periodic/open boundary condition along vertical/horizontal direction [c.f. Fig. 1(d) for a typical $YC4$ geometry]. We focus on the $3/4$ filling of the TBG flat bands with projected Coulomb interaction and correspondingly in Eq. (1) this means the electron number $\langle n_l (\equiv c_l^{\dagger} c_l) \rangle = 1/2$ with the valley and spin degrees of freedom polarized. Ref. [1] identified a CDW insulator and a topologically nontrivial QAH insulator in the ground state of the model, separated by a first-order transition at $\alpha \simeq 0.12$.

Here, we explore the finite- T properties of the TBG model with the XTRG method [63, 64], which constitutes an accurate many-body method at finite temperature, previously applied to simulate frustrated quantum magnets [71–73] as well as correlated fermions at both half filling and finite doping [74]. We retain up to $D = 1000$ states, which renders the truncation errors $\delta < 10^{-4}$ down to low- T regime.

We also employ the Gaussian state theory and field-theoretical approach to obtain both thermal and dynamical properties. The thermal state is approximated by a Gaussian ansatz, i.e., the optimal mean-field state, where the order parameters (i.e., all the single particle correlation functions) minimizing the free energy can be obtained efficiently via a set of flow equations [75, 76]. The particle-hole excitation spectrum can be obtained via the fluctuation analysis [77], or alternatively the analytic structure of the scattering T -matrix, i.e., the renormalized electronic interaction [c.f. the ladder diagram in Fig. 1(e)]. As the temperature increases, the interaction is strongly renormalized, which drastically modifies the self-energy [c.f. the Hartree-Fock-like contribution in Fig. 1(f)] of the single particle Green function. More details on methodologies are presented in the Supplemental Materials (SM) [85].

Finite-temperature phase diagram.— Fig. 2(a) summarizes our finite- T phase diagram, where the low- T phases include the CDW and QAH states, and the symmetric phase can be divided into two regimes, with the orange intermediate- T one acquiring pronounced collective (exciton) excitations and the red high- T state being trivial. As we will show below, there is a crossover between the intermediate- T and high- T regimes, while the intermediate- T and low- T phases are separated by a second-order phase transition of Ising universality. Moreover, the two low- T phases, i.e., the CDW and QAH ones, are separated by a first-order transition extending from the transition point $\alpha \simeq 0.12$ found in previous DMRG study [1].

In Fig. 3(a), the specific heat c_V shows pronounced peaks around $T_c \simeq 0.041$ for $\alpha = 0.2$, indicating the existence of

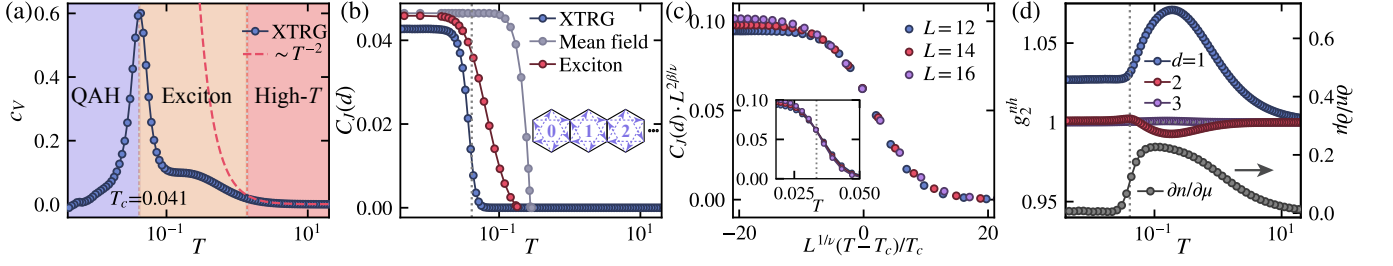


FIG. 3. For the case of $\alpha = 0.2$, (a) shows the specific heat c_V data, where the peak at $T_c = 0.041$ signifies the thermal phase transition. (b) Current-current correlation at a distance of $d = 6$, i.e. $C_J(d = 6)$ vs. T . Here, the XTRG and mean-field, as well as the field-theoretical results (Exciton) are shown. (c) Data collapse of the scaled current correlation $C_J(d = 6)$ versus $L^{1/\nu}(T - T_c)/T_c$ with the Ising critical exponents $\beta = \frac{1}{8}$ and $\nu = 1$, for the various system sizes. Insets show the $C \cdot L^{2\beta/\nu}$ versus temperature T , where the crossing point between different curves signifies the transition temperature T_c . The left axis of panel (d) shows the particle-hole correlation $g_2^{nh}(\mathbf{r})$ correlations with the reference site fixed at the center of the system denoted as the asterisk and $\mathbf{r} = d(\delta_1 - \delta_2)$ denoted in Fig. 1(d). The right axis of panel (d) shows the compressibility $\partial n/\partial\mu$ vs. T . The dashed lines in Panels (b,d) indicate the specific heat peak $T_c = 0.041$.

second-order phase transitions. The lower phase boundaries in Fig. 2(b) are drawn in this way by performing different α scans. The crossover line between the intermediate- and high- T regime is estimated by collecting the temperature where the c_V curve starts to scale as the high- T limit of T^{-2} [c.f. the red dashed line in Fig. 3(a)] [85].

Melting of the QAH and CDW states.— To detect the QAH phase, we calculate the current correlation, $C_J(d) = \langle J_0 J_d \rangle$, where $J_0 \equiv \frac{1}{6} \sum_{l \in \odot_0} i(c_l^\dagger c_{l+2} - \text{H.c.})/2$ is the average of all the next-nearest-neighbor (NNN) currents [c.f. purple dashed arrows in the inset of Fig. 3(b)] inside the selected hexagon \odot_0 in the $L/4$ -th column of the cylinder, and \odot_d is the d -th hexagon to the right of \odot_0 . We find $C_J(d)$ is nearly a constant in d inside the QAH state [85], indicating the existence of a long-range order. For $T > T_c$, $C_J(d)$ decays exponentially with d . In Fig. 3(b) we show the current correlation at a sufficiently long distance in the QAH state, i.e., $C_J(d = 6)$ versus T , which quickly drops and indicates the vanishing of QAH order above the c_V peak $T_c \simeq 0.041$. Notably, the mean-field results [depicted as the grey dots] overestimate the transition temperature T_c while the field theoretical calculation including the contribution of exciton to the quasiparticle self-energy, gives rise to $C_J(d)$ closer to the XTRG results, and together they agree with the corresponding temperature scale observed in the TBG experiment on the melting of the QAH order [9, 15]. By repeating the calculations of $C_J(d)$ for a wide range of α , we identify the existence of QAH phase with $\alpha > \alpha_c \simeq 0.12$ in the T - α plane as shown in Fig. 2(d). Following the similar procedure, but using the charge structure factor $C_n(\mathbf{M}) \equiv \frac{1}{N} \sum_i e^{-i\mathbf{M} \cdot \mathbf{r}_{oi}} (\langle \hat{n}_i \hat{n}_0 \rangle - \langle \hat{n}_i \rangle \langle \hat{n}_0 \rangle)$ at $\mathbf{M} \equiv (0, \pm \frac{2\pi}{\sqrt{3}})$, we identify the CDW phase in the left-bottom corner of the T - α plane, as shown in Fig. 2(c).

Next, we address the universality class of the phase transition by finite-size data collapsing of the current correlation $C_J(t, L)$ at $d = 6$ with $t \equiv (T - T_c)/T_c$. In the vicinity of the critical point, we have $C(t, L) = L^{-2\beta/\nu} g(tL^{1/\nu})$, where the scaling function behaves $g(x) \sim x^\beta$ as $x \rightarrow \infty$. As the low- T phase breaks Z_2 (TRS) symmetry, it is natural to expect a 2D

Ising universality class. To verify this, the critical exponents $\beta = 1/8$ and $\nu = 1$ of the order parameter and correlation length, respectively, are used to collapse the finite- T data in Fig. 3(c). In the inset of Fig. 3(c), we plotted the $C_J L^{2\beta/L}$ versus T and identify the critical temperature $T_c \simeq 0.034$ as the crossing points between curves of different system sizes. This is the T_c at the thermodynamic limit and slightly different from the peak in the specific peak in Fig. 3(a) for one system size. Then we rescale the x -axes as $tL^{1/\nu}$ and thus see perfect data collapses within the critical regimes in the main panels of Fig. 3(c).

Electron-hole correlation and exciton proliferation.— As temperature rises above T_c , the excitons proliferate and result in nontrivial features on the charge correlations. As shown in Fig. 1(d) with $T = 0.244$ and $\alpha = 0.2$, we place a hole at the very center of the lattice, and find electrons exhibit bunching and anti-bunching modulation behaviors as moving away from the hole, evidencing the existence of particle-hole bound states — excitons — in the system. Such peculiar charge correlations can be quantitatively reflected in the electron-hole correlator $g_2^{nh}(d) = \frac{\langle \hat{n}_0 \hat{h}_i \rangle}{\langle \hat{n}_0 \rangle \langle \hat{h}_i \rangle}$, with $\hat{h}_i = 1 - \hat{n}_i$ and measured between two sites (“0” and “i”) separated by distances $\mathbf{r} = d(\delta_1 - \delta_2)$ [c.f. Fig. 3(d)], which show increasing correlation whose “sign” changes for different distance in the regime $T > T_c$, and shows extremum values at an intermediate temperature $T_{\text{ex}} \simeq 0.3$ (around the mean-field transition temperature), at which the excitons can be easily excited since the single-particle gap now roughly equals the thermal energy scale. The electrons and holes at nearest sites belonging to the same sublattice [i.e., connected via $(\delta_1 - \delta_2)$ as shown in Fig. 1(d)] attract each other, while at further distance like $d = 2$ they repeal, reflecting the strong influence of excitons in the thermal states. As distance further enhances, e.g., $d = 3$, the electron-hole correlations become rather weak, showing that the excitons are indeed quite local. We note that, the charge correlation decays exponentially with distance, and thus the oscillation behavior is not attributed to Friedel oscillations. When the temperature further elevates and goes beyond

T_{ex} , even the short-range charge correlations get smeared by strong thermal fluctuations, all correlations decay ($g_2^{nh} \rightarrow 1$) at about $T_h \simeq 1$. Above this crossover temperature, i.e., in the high- T regime, specific heat c_V exhibit $\sim 1/T^2$ scaling as illustrated in Fig. 3(a) [85].

We also study the compressibility $\partial n/\partial\mu$ by adding a chemical potential term to the KV model [85]. In Fig. 3(d), the compressibility exhibits a steep jump above T_c and keeps an enhanced value inside the exciton regime. This is a direct result of the exciton proliferation above T_c , where the formation of excitons (bosonic bound state) significantly enhanced the compressibility. Such a steep enhancement can be measured in the quantum capacitance and scanning single electron transistor experiments [68–70]. In fact, the compressibility enhancement above the correlated insulators (CDW and QAH phases), is qualitatively consistent with the experimental observation at the same $3/4$ filling of TBG [70].

Dynamical signature of excitons.— At the mean-field level, the gap between the conductive and valence bands (white dots in Fig. 4 (a)) in the QAH phase is about $0.5U_0$ (at the Γ point in BZ), giving rise to a transition to the disorder phase at much higher temperature $T_c \sim 0.2$ (of the scale of 100 K for realistic materials), at the scale of the ground state band gap [1]. However, our XTRG computation finds a much lower transition temperature $T_c \sim 0.04$ (~ 10 K) by one order of magnitude, which agrees with the experimental results [9, 15] implying the failure of the mean-field theory at finite temperatures.

To explore the mechanism of such low transition temperature, we perform the diagrammatic calculation (see details in SM [85]) on the T -matrix in the particle-hole channel and its correction to the self-energy of single-particle Green functions. The poles of the T -matrix determine the exciton spectrum. As shown by the green diamonds in Fig. 4 (a) at a representative temperature $T = 0.08$, the exciton has a much lower energy $E_{\text{ex}} \sim 0.08$ than the mean-field gap. As a result, at the finite temperature comparable with E_{ex} , many excitons are proliferated by thermal fluctuations, and the scattering with excitons strongly affects single electron behaviors in conductive and valence bands. The effect of excitons to the single particle Green function can be characterized by the T -matrix in the Hartree-Fock correction to the self energy (Fig. 1(e) and (f)). In Fig. 4 (a), we show such renormalized spectral function $A_{\mathbf{k}}^{c,v}(\omega)$ for electrons in conductive and valence bands at $T = 0.08$, which displays much smaller band gap than that from the mean-field theory. In Fig. 4(b,c), the spectral functions of electrons in the valence band at different temperatures show the reduced quasi-particle weight and the broadened peak as T increases. It is remarkable that at the temperature inside the exciton regime, the collective mode assists the valence electron to tunnel across the band gap and redistribute in the positive frequency region. This intriguing feature is the signature of the electron dressed by the cloud of proliferated excitons, which can be probed via spectroscopy. The absorption spectra of probe light display peaks at the exciton frequencies (~ 100 GHz shown in Fig. 4). Due to the

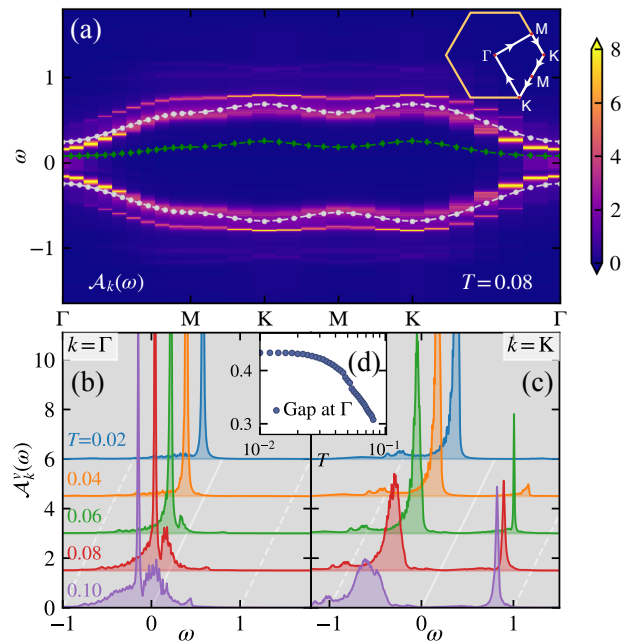


FIG. 4. (a) Quasi-particle spectral function $\mathcal{A}_{\mathbf{k}}(\omega) = \mathcal{A}_{\mathbf{k}}^v(\omega) + \mathcal{A}_{\mathbf{k}}^c(\omega)$ as the sum of valence and conducting band spectrum, for $\alpha = 0.2$ at $T = 0.08$, where the spectral weight distribution gets broadened as compared to the mean-field single-particle dispersion consisted of upper conducting and lower valence bands (white dots). The exciton band lying within the single-particle gap is denoted by green diamonds. The inset depicts the path in the Brillouin zone. Panels (b,c) show the valence electron spectral weights at $k = \Gamma$ and $k = K$ for various temperatures, where the values of \mathcal{A} and ω are properly shifted as indicated by the tilted white lines. (d) shows the gap, defined as twice the peak position of $\mathcal{A}_{\Gamma}^v(\omega)$, as a function of temperature T .

strong exciton dressing, the current correlation function is thus highly reduced, as shown by the red dots in Fig. 3 (b). Accompanied with the results in Figs. 1 (d) and 3 (d), our results provide a direct observation of proliferated excitations in the $3/4$ filling setting of TBG model. We also confirm, a small kinetic term will not qualitatively change the exciton physics observed here [85].

Discussion.— We extend the studies of the TBG model to the finite-temperature properties and collective excitations. In particular, the excitons formed by a pair of quasi-particle and hole proliferate at intermediate temperatures, which significantly influences the charge correlations and provide a mechanism to melt the QAH phase. We therefore reconcile the large quasi-particle band gap and small QAH transition temperature observed in experiments. The excitons, as collective excitations due to Coulomb interactions, have been investigated and discussed in bilayer graphene [78, 79], TBG [67, 80], as well as the recent observation of the QAH in TMD heterobilayers [34]. We note that, the exciton physics here is a distinct feature of flat-band system, different from the Haldane-Hubbard model (see, e.g., Ref. [83]) where the excitons comprised of band electrons and holes do not experience a prolif-

eration upon rising temperature [85]. Our work here shows the emergence of excitons in the strong coupling limit in a TBG lattice model, proposing intriguing exciton physics such as the charge compressibility and the spectral fingerprint in both single-particle and collective models, waiting to be explored in future experiments of quantum moiré systems. We point out that, the valley and spin degrees of freedom, which may give rise to other neutral collective modes (e.g. magnon) and possible Pomeranchuk physics, are omitted in the present model and will be addressed in a future study.

Acknowledgments.— X.Y.L. and B.B.C. contributed equally to this work. X.Y.L., W.L., Z.Y.M. and T.S. are indebted to Jian Kang and Yifan Qu for stimulating discussions. X.Y.L., W.L. and T.S. acknowledge the support from the NSFC through Grant Nos. 11974036, 11834014, 11974363 and 12047503. B.B.C. and Z.Y.M. acknowledge support from the RGC of Hong Kong SAR of China (Grant Nos. 17303019, 17301420, 17301721 and AoE/P-701/20), the Strategic Priority Research Program of the Chinese Academy of Sciences (Grant No. XDB33000000), the K. C. Wong Education Foundation (Grant No. GJTD-2020-01) and the Seed Funding "Quantum-Inspired explainable-AI" at the HKU-TCL Joint Research Centre for Artificial Intelligence. We thank the High-performance Computing Center at ITP-CAS, the Computational Initiative at the Faculty of Science and Information Technology Service at the University of Hong Kong, and the Tianhe platforms at the National Super-computer Centers for their technical support and generous allocation of CPU time.

* bchenhku@hku.hk

† zymeng@hku.hk

‡ tshi@itp.ac.cn

- [1] B.-B. Chen, Y. D. Liao, Z. Chen, O. Vafek, J. Kang, W. Li, and Z. Y. Meng, "Realization of topological Mott insulator in a twisted bilayer graphene lattice model," *Nat Commun* **12**, 5480 (2021).
- [2] Y. Cao, V. Fatemi, A. Demir, S. Fang, S. L. Tomarken, J. Y. Luo, J. D. Sanchez-Yamagishi, K. Watanabe, T. Taniguchi, E. Kaxiras, R. C. Ashoori, and P. Jarillo-Herrero, "Correlated insulator behaviour at half-filling in magic-angle graphene superlattices," *Nature* **556**, 80 (2018).
- [3] Y. Cao, V. Fatemi, S. Fang, K. Watanabe, T. Taniguchi, E. Kaxiras, and P. Jarillo-Herrero, "Unconventional superconductivity in magic-angle graphene superlattices," *Nature* **556**, 43 (2018).
- [4] G. Trambly de Laissardière, D. Mayou, and L. Magaud, "Localization of dirac electrons in rotated graphene bilayers," *Nano Letters* **10**, 804–808 (2010), pMID: 20121163.
- [5] G. Trambly de Laissardière, D. Mayou, and L. Magaud, "Numerical studies of confined states in rotated bilayers of graphene," *Phys. Rev. B* **86**, 125413 (2012).
- [6] R. Bistritzer and A. H. MacDonald, "Moiré bands in twisted double-layer graphene," *Proceedings of the National Academy of Sciences* **108**, 12233–12237 (2011).
- [7] M. Yankowitz, S. Chen, H. Polshyn, Y. Zhang, K. Watanabe, T. Taniguchi, D. Graf, A. F. Young, and C. R. Dean, "Tuning superconductivity in twisted bilayer graphene," *Science* **363**, 1059–1064 (2019).
- [8] X. Lu, P. Stepanov, W. Yang, M. Xie, M. A. Aamir, I. Das, C. Urgell, K. Watanabe, T. Taniguchi, G. Zhang, A. Bachtold, A. H. MacDonald, and D. K. Efetov, "Superconductors, orbital magnets, and correlated states in magic angle bilayer graphene," *Nature* **574**, 653–657 (2019).
- [9] A. L. Sharpe, E. J. Fox, A. W. Barnard, J. Finney, K. Watanabe, T. Taniguchi, M. A. Kastner, and D. Goldhaber-Gordon, "Emergent ferromagnetism near three-quarters filling in twisted bilayer graphene," *Science* **365**, 605–608 (2019).
- [10] G. Chen, A. L. Sharpe, E. J. Fox, Y.-H. Zhang, S. Wang, L. Jiang, B. Lyu, H. Li, K. Watanabe, T. Taniguchi, *et al.*, "Tunable correlated chern insulator and ferromagnetism in a moiré superlattice," *Nature* **579**, 56–61 (2020).
- [11] A. Kerelsky, L. J. McGilly, D. M. Kennes, L. Xian, M. Yankowitz, S. Chen, K. Watanabe, T. Taniguchi, J. Hone, C. Dean, *et al.*, "Maximized electron interactions at the magic angle in twisted bilayer graphene," *Nature* **572**, 95–100 (2019).
- [12] S. L. Tomarken, Y. Cao, A. Demir, K. Watanabe, T. Taniguchi, P. Jarillo-Herrero, and R. C. Ashoori, "Electronic compressibility of magic-angle graphene superlattices," *Phys. Rev. Lett.* **123**, 046601 (2019).
- [13] Y. Xie, B. Lian, B. Jäck, X. Liu, C.-L. Chiu, K. Watanabe, T. Taniguchi, B. A. Bernevig, and A. Yazdani, "Spectroscopic signatures of many-body correlations in magic-angle twisted bilayer graphene," *Nature* **572**, 101–105 (2019).
- [14] C. Shen, Y. Chu, Q. Wu, N. Li, S. Wang, Y. Zhao, J. Tang, J. Liu, J. Tian, K. Watanabe, T. Taniguchi, R. Yang, Z. Y. Meng, D. Shi, O. V. Yazyev, and G. Zhang, "Correlated states in twisted double bilayer graphene," *Nature Physics* (2020), [10.1038/s41567-020-0825-9](https://doi.org/10.1038/s41567-020-0825-9).
- [15] M. Serlin, C. L. Tschirhart, H. Polshyn, Y. Zhang, J. Zhu, K. Watanabe, T. Taniguchi, L. Balents, and A. F. Young, "Intrinsic quantized anomalous Hall effect in a moiré heterostructure," *Science* **367**, 900–903 (2020).
- [16] K. P. Nuckolls, M. Oh, D. Wong, B. Lian, K. Watanabe, T. Taniguchi, B. A. Bernevig, and A. Yazdani, "Strongly correlated chern insulators in magic-angle twisted bilayer graphene," *Nature* **588**, 610–615 (2020).
- [17] A. T. Pierce, Y. Xie, J. M. Park, E. Khalaf, S. H. Lee, Y. Cao, D. E. Parker, P. R. Forrester, S. Chen, K. Watanabe, T. Taniguchi, A. Vishwanath, P. Jarillo-Herrero, and A. Yacoby, "Unconventional sequence of correlated chern insulators in magic-angle twisted bilayer graphene," (2021), [arXiv:2101.04123 \[cond-mat.mes-hall\]](https://arxiv.org/abs/2101.04123).
- [18] S. Moriyama, Y. Morita, K. Komatsu, K. Endo, T. Iwasaki, S. Nakaharai, Y. Noguchi, Y. Wakayama, E. Watanabe, D. Tsuya, K. Watanabe, and T. Taniguchi, "Observation of superconductivity in bilayer graphene/hexagonal boron nitride superlattices," *arXiv e-prints*, [arXiv:1901.09356](https://arxiv.org/abs/1901.09356) (2019), [arXiv:1901.09356 \[cond-mat.supr-con\]](https://arxiv.org/abs/1901.09356).
- [19] A. Rozen, J. M. Park, U. Zondiner, Y. Cao, D. Rodan-Legrain, T. Taniguchi, K. Watanabe, Y. Oreg, A. Stern, E. Berg, P. Jarillo-Herrero, and S. Ilani, "Entropic evidence for a pomeranchuk effect in magic-angle graphene," *Nature* **592**, 214–219 (2021).
- [20] Y. Saito, F. Yang, J. Ge, X. Liu, T. Taniguchi, K. Watanabe, J. I. A. Li, E. Berg, and A. F. Young, "Isospin pomeranchuk effect in twisted bilayer graphene," *Nature* **592**, 220–224 (2021).
- [21] X. Liu, C.-L. Chiu, J. Y. Lee, G. Farahi, K. Watanabe, T. Taniguchi, A. Vishwanath, and A. Yazdani, "Spectroscopy of a Tunable Moiré System with a Correlated and Topological Flat Band," *arXiv preprint arXiv:2008.07552* (2020).

- [22] M. H. Naik and M. Jain, “Ultraflatbands and shear solitons in moiré patterns of twisted bilayer transition metal dichalcogenides,” *Phys. Rev. Lett.* **121**, 266401 (2018).
- [23] F. Conte, D. Ninno, and G. Cantele, “Electronic properties and interlayer coupling of twisted MoS₂/NbSe₂ heterobilayers,” *Phys. Rev. B* **99**, 155429 (2019).
- [24] Y. Tang, L. Li, T. Li, Y. Xu, S. Liu, K. Barmak, K. Watanabe, T. Taniguchi, A. H. MacDonald, J. Shan, and K. F. Mak, “Simulation of Hubbard model physics in WSe₂/WS₂ moiré superlattices,” *Nature* **579**, 353–358 (2020).
- [25] L. Xian, M. Claassen, D. Kiese, M. M. Scherer, S. Trebst, D. M. Kennes, and A. Rubio, “Realization of Nearly Dispersionless Bands with Strong Orbital Anisotropy from Destructive Interference in Twisted Bilayer MoS₂,” *ArXiv:2004.02964 Cond-Mat* (2020), [arXiv:2004.02964 \[cond-mat\]](https://arxiv.org/abs/2004.02964).
- [26] H. Pan, F. Wu, and S. Das Sarma, “Band topology, Hubbard model, Heisenberg model, and Dzyaloshinskii-Moriya interaction in twisted bilayer WSe₂,” *Phys. Rev. Research* **2**, 033087 (2020).
- [27] S. Venkateswarlu, A. Honecker, and G. Trambly de Laissardière, “Electronic localization in twisted bilayer MoS₂ with small rotation angle,” *Phys. Rev. B* **102**, 081103 (2020).
- [28] Z. Lu, S. Carr, D. T. Larson, and E. Kaxiras, “Lithium intercalation in MoS₂ bilayers and implications for moiré flat bands,” *Phys. Rev. B* **102**, 125424 (2020).
- [29] Z. Zhang, Y. Wang, K. Watanabe, T. Taniguchi, K. Ueno, E. Tutuc, and B. J. LeRoy, “Flat bands in twisted bilayer transition metal dichalcogenides,” *Nat. Phys.* **16**, 1093–1096 (2020).
- [30] I. Maity, P. K. Maiti, H. R. Krishnamurthy, and M. Jain, “Reconstruction of moiré lattices in twisted transition metal dichalcogenide bilayers,” *Phys. Rev. B* **103**, L121102 (2021), [arXiv:1912.08702](https://arxiv.org/abs/1912.08702).
- [31] X. Zhang, G. Pan, Y. Zhang, J. Kang, and Z. Y. Meng, “Momentum Space Quantum Monte Carlo on Twisted Bilayer Graphene,” *Chinese Physics Letters* **38**, 077305 (2021).
- [32] G. Pan, X. Zhang, H. Li, K. Sun, and Z. Y. Meng, “Dynamic properties of collective excitations in twisted bilayer Graphene,” *arXiv e-prints*, [arXiv:2108.12559](https://arxiv.org/abs/2108.12559) (2021), [arXiv:2108.12559 \[cond-mat.str-el\]](https://arxiv.org/abs/2108.12559).
- [33] X. Zhang, K. Sun, H. Li, G. Pan, and Z. Y. Meng, “Superconductivity and bosonic fluid emerging from Moiré flat bands,” *arXiv e-prints*, [arXiv:2111.10018](https://arxiv.org/abs/2111.10018) (2021), [arXiv:2111.10018 \[cond-mat.supr-con\]](https://arxiv.org/abs/2111.10018).
- [34] T. Li, S. Jiang, B. Shen, Y. Zhang, L. Li, T. Devakul, K. Watanabe, T. Taniguchi, L. Fu, J. Shan, and K. F. Mak, “Quantum anomalous Hall effect from intertwined moiré bands,” *arXiv e-prints*, [arXiv:2107.01796](https://arxiv.org/abs/2107.01796) (2021), [arXiv:2107.01796 \[cond-mat.mes-hall\]](https://arxiv.org/abs/2107.01796).
- [35] H. Li, U. Kumar, K. Sun, and S.-Z. Lin, “Spontaneous fractional Chern insulators in transition metal dichalcogenides Moire superlattices,” *arXiv e-prints*, [arXiv:2101.01258](https://arxiv.org/abs/2101.01258) (2021), [arXiv:2101.01258 \[cond-mat.mes-hall\]](https://arxiv.org/abs/2101.01258).
- [36] Y.-M. Xie, C.-P. Zhang, J.-X. Hu, K. F. Mak, and K. T. Law, “Theory of Valley Polarized Quantum Anomalous Hall State in Moiré MoTe₂/WSe₂ Heterobilayers,” *arXiv e-prints*, [arXiv:2106.13991](https://arxiv.org/abs/2106.13991) (2021), [arXiv:2106.13991 \[cond-mat.mes-hall\]](https://arxiv.org/abs/2106.13991).
- [37] S. Wu, Z. Zhang, K. Watanabe, T. Taniguchi, and E. Y. Andrei, “Chern insulators, van Hove singularities and topological flat bands in magic-angle twisted bilayer graphene,” *Nature Materials* **20**, 488–494 (2021).
- [38] I. Das, X. Lu, J. Herzog-Arbeitman, Z.-D. Song, K. Watanabe, T. Taniguchi, B. A. Bernevig, and D. K. Efetov, “Symmetry-broken Chern insulators and Rashba-like Landau-level crossings in magic-angle bilayer graphene,” *Nature Physics* **17**, 710–714 (2021).
- [39] H. C. Po, L. Zou, T. Senthil, and A. Vishwanath, “Faithful tight-binding models and fragile topology of magic-angle bilayer graphene,” *Phys. Rev. B* **99**, 195455 (2019).
- [40] J. Liu, J. Liu, and X. Dai, “Pseudo Landau level representation of twisted bilayer graphene: Band topology and implications on the correlated insulating phase,” *Phys. Rev. B* **99**, 155415 (2019).
- [41] H. C. Po, L. Zou, A. Vishwanath, and T. Senthil, “Origin of Mott insulating behavior and superconductivity in twisted bilayer graphene,” *Phys. Rev. X* **8**, 031089 (2018).
- [42] H. C. Po, H. Watanabe, and A. Vishwanath, “Fragile Topology and Wannier Obstructions,” *Phys. Rev. Lett.* **121**, 126402 (2018).
- [43] J. Liu and X. Dai, “Theories for the correlated insulating states and quantum anomalous Hall effect phenomena in twisted bilayer graphene,” *Phys. Rev. B* **103**, 035427 (2021).
- [44] J. Liu, Z. Ma, J. Gao, and X. Dai, “Quantum Valley Hall Effect, Orbital Magnetism, and Anomalous Hall Effect in Twisted Multilayer Graphene Systems,” *Phys. Rev. X* **9**, 031021 (2019).
- [45] J. Liu and X. Dai, “Anomalous Hall effect, magneto-optical properties, and nonlinear optical properties of twisted graphene systems,” *npj Computational Materials* **6**, 57 (2020).
- [46] N. Bultinck, E. Khalaf, S. Liu, S. Chatterjee, A. Vishwanath, and M. P. Zaletel, “Ground state and hidden symmetry of magic-angle graphene at even integer filling,” *Phys. Rev. X* **10**, 031034 (2020).
- [47] N. Bultinck, S. Chatterjee, and M. P. Zaletel, “Mechanism for Anomalous Hall Ferromagnetism in Twisted Bilayer Graphene,” *Phys. Rev. Lett.* **124**, 166601 (2020).
- [48] B. A. Bernevig, Z.-D. Song, N. Regnault, and B. Lian, “Twisted bilayer graphene. I. Matrix elements, approximations, perturbation theory, and a $k \cdot p$ two-band model,” *Phys. Rev. B* **103**, 205411 (2021).
- [49] Z.-D. Song, B. Lian, N. Regnault, and B. A. Bernevig, “Twisted bilayer graphene. II. Stable symmetry anomaly,” *Phys. Rev. B* **103**, 205412 (2021).
- [50] B. A. Bernevig, Z.-D. Song, N. Regnault, and B. Lian, “Twisted bilayer graphene. III. Interacting Hamiltonian and exact symmetries,” *Phys. Rev. B* **103**, 205413 (2021).
- [51] B. Lian, Z.-D. Song, N. Regnault, D. K. Efetov, A. Yazdani, and B. A. Bernevig, “Twisted bilayer graphene. IV. Exact insulator ground states and phase diagram,” *Phys. Rev. B* **103**, 205414 (2021).
- [52] B. A. Bernevig, B. Lian, A. Cowsik, F. Xie, N. Regnault, and Z.-D. Song, “Twisted bilayer graphene. V. Exact analytic many-body excitations in Coulomb Hamiltonians: Charge gap, Goldstone modes, and absence of Cooper pairing,” *Phys. Rev. B* **103**, 205415 (2021).
- [53] F. Xie, A. Cowsik, Z.-D. Song, B. Lian, B. A. Bernevig, and N. Regnault, “Twisted bilayer graphene. VI. An exact diagonalization study at nonzero integer filling,” *Phys. Rev. B* **103**, 205416 (2021).
- [54] J. Kang and O. Vafek, “Strong coupling phases of partially filled twisted bilayer graphene narrow bands,” *Phys. Rev. Lett.* **122**, 246401 (2019).
- [55] X. Zhang, G. Pan, X. Y. Xu, and Z. Y. Meng, “Sign Problem Finds Its Bounds,” *arXiv e-prints*, [arXiv:2112.06139](https://arxiv.org/abs/2112.06139) (2021), [arXiv:2112.06139 \[cond-mat.str-el\]](https://arxiv.org/abs/2112.06139).
- [56] J. Kang and O. Vafek, “Symmetry, maximally localized wannier states, and a low-energy model for twisted bilayer graphene narrow bands,” *Phys. Rev. X* **8**, 031088 (2018).
- [57] X. Y. Xu, K. T. Law, and P. A. Lee, “Kekulé valence bond

- order in an extended hubbard model on the honeycomb lattice with possible applications to twisted bilayer graphene,” *Phys. Rev. B* **98**, 121406 (2018).
- [58] Y. Da Liao, Z. Y. Meng, and X. Y. Xu, “Valence Bond Orders at Charge Neutrality in a Possible Two-Orbital Extended Hubbard Model for Twisted Bilayer Graphene,” *Phys. Rev. Lett.* **123**, 157601 (2019).
- [59] Y. Da Liao, J. Kang, C. N. Breiø, X. Y. Xu, H.-Q. Wu, B. M. Andersen, R. M. Fernandes, and Z. Y. Meng, “Correlation-induced insulating topological phases at charge neutrality in twisted bilayer graphene,” *Phys. Rev. X* **11**, 011014 (2021).
- [60] Y.-D. Liao, X.-Y. Xu, Z.-Y. Meng, and J. Kang, “Correlated insulating phases in the twisted bilayer graphene,” *Chinese Physics B* **30**, 017305 (2021).
- [61] S. Raghu, X.-L. Qi, C. Honerkamp, and S.-C. Zhang, “Topological Mott Insulators,” *Phys. Rev. Lett.* **100**, 156401 (2008).
- [62] J. Liu and X. Dai, “Anomalous Hall effect, magneto-optical properties, and nonlinear optical properties of twisted graphene systems,” *npj Computational Materials* **6**, 57 (2020).
- [63] B.-B. Chen, L. Chen, Z. Chen, W. Li, and A. Weichselbaum, “Exponential thermal tensor network approach for quantum lattice models,” *Phys. Rev. X* **8**, 031082 (2018).
- [64] H. Li, B.-B. Chen, Z. Chen, J. von Delft, A. Weichselbaum, and W. Li, “Thermal tensor renormalization group simulations of square-lattice quantum spin models,” *Phys. Rev. B* **100**, 045110 (2019).
- [65] E. Khalaf, N. Bultinck, A. Vishwanath, and M. P. Zaletel, “Soft modes in magic angle twisted bilayer graphene,” arXiv e-prints, arXiv:2009.14827 (2020), arXiv:2009.14827 [cond-mat.str-el].
- [66] O. Vafek and J. Kang, “Lattice model for the Coulomb interacting chiral limit of the magic angle twisted bilayer graphene: symmetries, obstructions and excitations,” arXiv e-prints, arXiv:2106.05670 (2021), arXiv:2106.05670 [cond-mat.str-el].
- [67] Y. H. Kwan, Y. Hu, S. H. Simon, and S. A. Parameswaran, “Exciton band topology in spontaneous quantum anomalous hall insulators: Applications to twisted bilayer graphene,” *Phys. Rev. Lett.* **126**, 137601 (2021).
- [68] J. P. Eisenstein, L. N. Pfeiffer, and K. W. West, “Negative compressibility of interacting two-dimensional electron and quasi-particle gases,” *Phys. Rev. Lett.* **68**, 674–677 (1992).
- [69] D. Wong, K. P. Nuckolls, M. Oh, B. Lian, Y. Xie, S. Jeon, K. Watanabe, T. Taniguchi, B. A. Bernevig, and A. Yazdani, “Cascade of electronic transitions in magic-angle twisted bilayer graphene,” *Nature* **582**, 198–202 (2020).
- [70] U. Zondiner, A. Rozen, D. Rodan-Legrain, Y. Cao, R. Queiroz, T. Taniguchi, K. Watanabe, Y. Oreg, F. von Oppen, A. Stern, *et al.*, “Cascade of phase transitions and dirac revivals in magic-angle graphene,” *Nature* **582**, 203–208 (2020).
- [71] L. Chen, D.-W. Qu, H. Li, B.-B. Chen, S.-S. Gong, J. von Delft, A. Weichselbaum, and W. Li, “Two temperature scales in the triangular lattice Heisenberg antiferromagnet,” *Phys. Rev. B* **99**, 140404(R) (2019).
- [72] H. Li, Y. D. Liao, B.-B. Chen, X.-T. Zeng, X.-L. Sheng, Y. Qi, Z. Y. Meng, and W. Li, “Kosterlitz-Thouless melting of magnetic order in the triangular quantum Ising material TmMgGaO_4 ,” *Nat. Commun.* **11**, 1111 (2020).
- [73] H. Li, H.-K. Zhang, J. Wang, H.-Q. Wu, Y. Gao, D.-W. Qu, Z.-X. Liu, S.-S. Gong, and W. Li, “Identification of magnetic interactions and high-field quantum spin liquid in $\alpha\text{-RuCl}_3$,” *Nature Communications* **12**, 4007 (2021).
- [74] B.-B. Chen, C. Chen, Z. Chen, J. Cui, Y. Zhai, A. Weichselbaum, J. von Delft, Z. Y. Meng, and W. Li, “Quantum Many-Body Simulations of the Two-Dimensional Fermi-Hubbard Model in Ultracold Optical Lattices,” *Phys. Rev. B* **103**, L041107 (2021).
- [75] T. Shi, E. Demler, and J. Ignacio Cirac, “Variational study of fermionic and bosonic systems with non-gaussian states: Theory and applications,” *Annals of Physics* **390**, 245–302 (2018).
- [76] T. Shi, E. Demler, and J. I. Cirac, “Variational approach for many-body systems at finite temperature,” *Phys. Rev. Lett.* **125**, 180602 (2020).
- [77] T. Guaita, L. Hackl, T. Shi, C. Hubig, E. Demler, and J. I. Cirac, “Gaussian time-dependent variational principle for the bose-hubbard model,” *Phys. Rev. B* **100**, 094529 (2019).
- [78] L. Ju, L. Wang, T. Cao, T. Taniguchi, K. Watanabe, S. G. Louie, F. Rana, J. Park, J. Hone, F. Wang, and P. L. McEuen, “Tunable excitons in bilayer graphene,” *Science* **358**, 907–910 (2017).
- [79] F. Wu, T. Lovorn, and A. H. MacDonald, “Topological exciton bands in moiré heterojunctions,” *Phys. Rev. Lett.* **118**, 147401 (2017).
- [80] X. Liu, K. Watanabe, T. Taniguchi, B. I. Halperin, and P. Kim, “Quantum hall drag of exciton condensate in graphene,” *Nature Physics* **13**, 746–750 (2017).
- [81] H. F. Trotter, “On the product of semi-groups of operators,” *Proceedings of the American Mathematical Society* **10**, 545–551 (1959).
- [82] B.-B. Chen, Y.-J. Liu, Z. Chen, and W. Li, “Series-expansion thermal tensor network approach for quantum lattice models,” *Phys. Rev. B* **95**, 161104 (2017).
- [83] C. Shao, E. V. Castro, S. Hu, and R. Mondaini, “Interplay of local order and topology in the extended Haldane-Hubbard model,” *Phys. Rev. B* **103**, 035125 (2021).
- [84] F. D. M. Haldane, “Model for a Quantum Hall Effect without Landau Levels: Condensed-Matter Realization of the “Parity Anomaly”,” *Phys. Rev. Lett.* **61**, 2015–2018 (1988).
- [85] In Supplementary Materials Sec. I, we briefly summarized exponential tensor renormalization group method, its measurements on thermodynamic quantities, and adaption to fermion systems are introduced. Sec. II is devoted to the details of determination of crossover temperature between intermediate- T regime and the high- T regime. In Sec. III, we present the current correlation calculations. In Sec. IV, we discuss the thermodynamics of the system in the small- α regime. In Sec. V, we present more thermodynamic data for various α values. In Sec. VI, we include the electronic compressibility calculations. In Sec. VII and Sec. VIII, the Gaussian state approach and the implementation of perturbative field theoretical calculations on the single-particle and collective excitations are presented. In Sec. IX, we discuss the thermodynamics of Haldane-Hubbard model. The Supplementary Materials include references [1, 63, 64, 75, 76, 81–84].

SUPPLEMENTAL MATERIALS FOR
EXCITON PROLIFERATION AND FATE OF THE TOPOLOGICAL MOTT INSULATOR IN A
TWISTED BILAYER GRAPHENE LATTICE MODEL

Section I: Exponential Tensor Renormalization Group Method

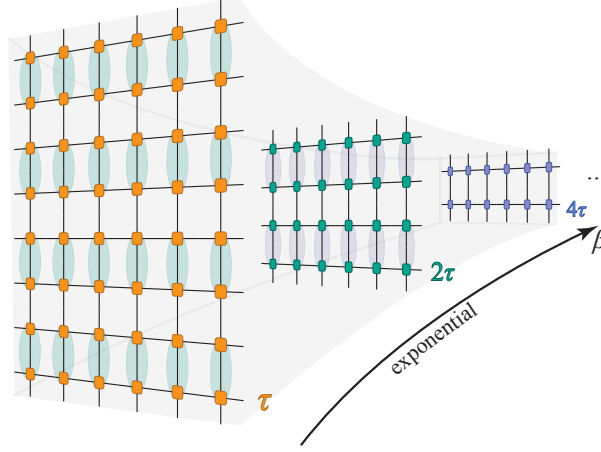


FIG. S1. Exponential evolution scheme in exponential tensor renormalization group (XTRG) method.

As shown in Fig. S1, the main idea of exponential tensor renormalization group (XTRG) [63, 64] method is, to first construct the initial high-temperature density operator $\hat{\rho}_0 \equiv \hat{\rho}(\tau) = e^{-\tau \hat{H}}$ with τ being an exponentially small inverse temperature, which can be obtained with ease via Trotter-Suzuki decomposition [81] or series-expansion methods [82]. Subsequently, we evolve the thermal state exponentially by squaring the density operator iteratively, i.e., $\hat{\rho}_n \cdot \hat{\rho}_n \equiv \hat{\rho}(2^n \tau) \cdot \hat{\rho}(2^n \tau) \rightarrow \hat{\rho}_{n+1}$. Following this exponential evolution scheme, one can significantly reduce the evolution as well as truncation steps, and thus can obtain highly accurate low- T data in greatly improved efficiency.

In XTRG simulations, we compute the internal energy per site

$$u(T) \equiv \frac{1}{N} \frac{\text{Tr}[H \cdot \rho(T)]}{\text{Tr}[\rho(T)]}, \quad (\text{S1})$$

where H is the Hamiltonian [c.f. Eq. (1)] and $\rho(T) \equiv e^{-H/T}$ is the density matrix of the system with N sites, and the specific heat via the derivative of internal energy, is

$$c_V(T) \equiv -\frac{\partial u(T)}{\partial T} = \frac{\partial u(\beta)}{\partial \ln \beta} \beta, \quad (\text{S2})$$

with $\beta \equiv 1/T$ the inverse temperature.

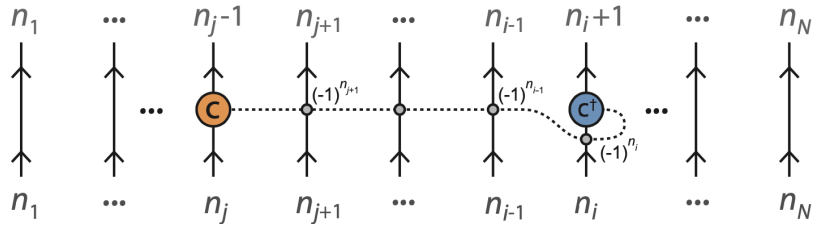


FIG. S2. Representation of one-body operator $c_i^\dagger c_j$ as a matrix product operator with bond dimension $D = 1$.

When adapting XTRG to fermion systems, one should take care of the fermionic sign of exchanging two electrons. In this work, we are working on the many-body basis $|n_1 n_2 \cdots n_N\rangle \equiv (c_N^\dagger)^{n_N} \cdots (c_2^\dagger)^{n_2} (c_1^\dagger)^{n_1} |\Omega\rangle$, where $n_i (\in \{0, 1\})$ is

the number of electrons at the site i and $|\Omega\rangle$ is the vacuum state. Generically in this basis, the one-body operator $c_i^\dagger c_j$ (assuming $j < i$) requires a sign $\prod_{l=j+1}^i (-1)^{n_l}$, in addition to transform the state $|n_1 \cdots n_j \cdots n_i \cdots n_N\rangle$ to the state $|n_1 \cdots n_{j-1} \cdots n_{i+1} \cdots n_N\rangle$. As shown in Fig. S2, such fermion-sign structure can be encoded in XTRG readily in a matrix product operator with bond dimension $D = 1$.

Section II: Crossover between exciton proliferation regime and high-T regime

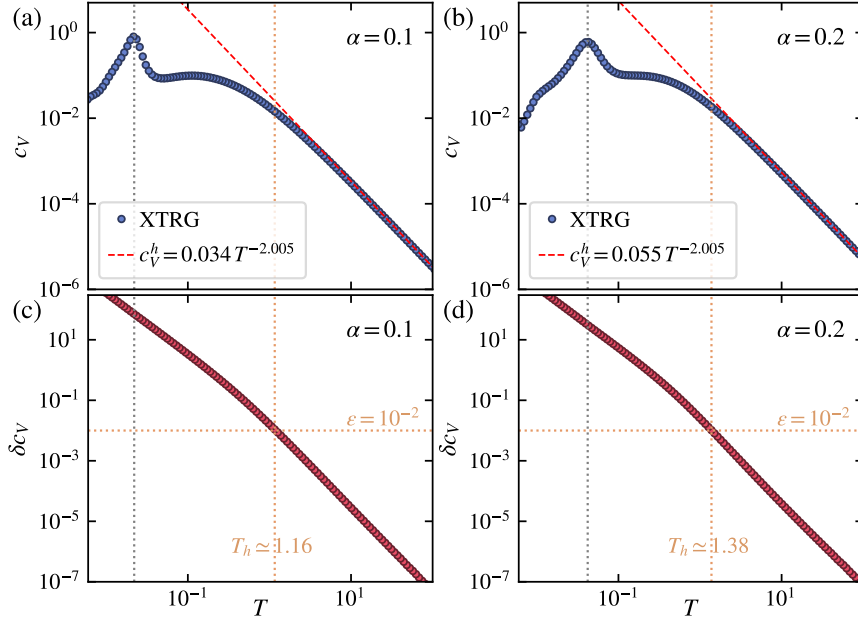


FIG. S3. In a YC4 \times 12 system for (a) $\alpha = 0.1$, and (b) $\alpha = 0.2$, specific heat c_V curves are shown versus temperature T in a double-logarithmic scale. At high-temperature limit, c_V behaves as $\sim T^{-2}$, and is fitted by the red dashed line c_V^h . Panels (c) and (d) show the deviation $\delta c_V = |c_V - c_V^h|$ as functions of temperature T . The crossover temperature between intermediate- T regime and the high- T one is determined by a threshold $\epsilon = 10^{-2}$.

In this section, we will discuss the determination of the crossover between the intermediate- T exciton proliferation regime and the high- T gas-like regime. In a high temperature $T = 1/\tau$ (i.e., a small inverse temperature τ), the internal energy density of the system

$$u(\tau) = \frac{1}{N} \frac{\text{Tr}[H \cdot \rho(\tau)]}{\text{Tr}[\rho(\tau)]} = \frac{1}{N} \frac{\text{Tr}(H \cdot e^{-\tau H})}{\text{Tr}(e^{-\tau H})},$$

via Taylor expansion, can be expressed as

$$u(\tau) = \frac{1}{N} \left[\frac{\text{Tr}(H)}{Z^0} - \frac{\text{Tr}(H^2)}{Z^0} \tau + \left(\frac{\text{Tr}(H)}{Z^0} \right)^2 \tau + O(\tau^2) \right].$$

Thus in the large- T limit, it yields

$$c_V \equiv \partial u / \partial T = (\partial u / \partial \tau) \cdot (\partial \tau / \partial T) \sim T^{-2}$$

for specific heat.

As shown in Fig. S3, we show the specific heat c_V of a YC4 \times 12 system at both $\alpha = 0.1$ and $\alpha = 0.2$, which show predominant power-law decay at high- T regime. As indicated by the red dashed lines in Fig. S3(a,b), we find the high- T data asymptotically follow $c_V^h = 0.034 T^{-2.005}$ and $c_V^h = 0.055 T^{-2.005}$ for $\alpha = 0.1$ and $\alpha = 0.2$ respectively, which are well consistent with the large- T limit. We thus determine the crossover temperature T_h between the high- T regime and intermediate- T regime, by computing the deviation of the specific heat from the high- T behavior, i.e., $\delta c_V = |c_V - c_V^h|$. To be more specific, we classify those temperatures at which $\delta c_V > \epsilon = 10^{-2}$ as intermediate- T , and otherwise as high- T .

Section III: Detailed current-current correlation calculation

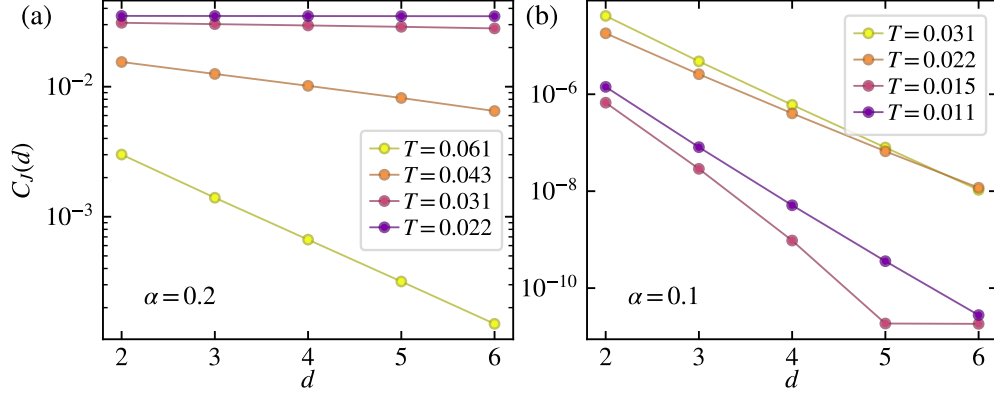


FIG. S4. In a $YC4 \times 12$ system for (a) $\alpha = 0.2$, and (b) $\alpha = 0.1$, the current-current correlation $C_J(d)$ is obtained versus distances d between hexagons, for various temperatures as indicated by the colored markers.

As shown in Fig. S4, we calculate the current-current correlation function $C_J(d)$, defined in the main text. In a $YC4 \times 12$ systems at $\alpha = 0.2$, C_J establish a plateau over distance d , in the quantum anomalous Hall (QAH) region, i.e., for $T < T_c \simeq 0.041$, whereas it decays exponentially for $T > T_c$. It means that, the lower- T region for the large α cases spontaneously break the time-reversal symmetry, manifesting the QAH state. On the other hand, for the small- α case ($\alpha = 0.1$ here), $C_J(d)$ decays exponentially for both regions of $T < T_c \simeq 0.022$ and $T > T_c$.

Section IV: More details on the CDW data

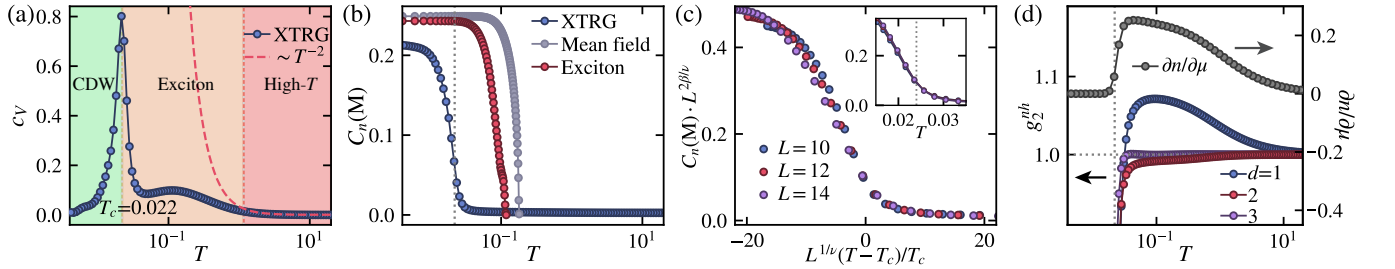


FIG. S5. (a) The specific heat c_V data are shown for $\alpha = 0.1$, where the peaks at $T_c = 0.022$ signify the thermal phase transitions. (b) Charge density structure factor $C_n(k) = \frac{1}{N} \sum_i e^{-ik \cdot r_{0i}} (\langle \hat{n}_i \hat{n}_0 \rangle - \langle \hat{n}_i \rangle \langle \hat{n}_0 \rangle)$ with $k = M$, vs. T for the $\alpha = 0.1$ case. Here, the XTRG and mean-field results are shown. (c) Data collapse of the scaled $C_n(M)$ versus $L^{1/\nu}(T - T_c)/T_c$ with the Ising critical exponents $\beta = \frac{1}{8}$ and $\nu = 1$, for the various system sizes. Insets show the $C \cdot L^{2\beta/\nu}$ versus temperature T , where the crossing point between curves of different system sizes signifies the thermodynamic limit transition temperature $T_c = 0.024$, slightly deviated from the specific heat peak at finite length $L = 12$. The left axis of panel (d) shows the particle-hole correlation $g_2^{ph}(\mathbf{r})$ correlations with the reference site fixed at the center of the system [c.f. Fig. 1(d) of the main text]. The right axis of panel (d) shows the compressibility $\partial n / \partial \mu$ vs. T . The dashed lines in Panels (b,d) indicate the specific heat peak $T_c = 0.022$.

In this section, we discuss more detailed thermodynamics results of the CDW phase for $\alpha < \alpha_c$. In Fig. S5(a), we show the specific heat c_V curve vs. temperature T , which peaks at $T_c \simeq 0.022$ predominantly, indicating a phase transition there. We also compute the density-density correlation function $\langle \hat{n}_i \hat{n}_0 \rangle \equiv \text{Tr}(\hat{\rho} \hat{n}_i \hat{n}_0)$ at various temperatures, with site 0 being fixed at a center site and site i running over the lattice. The charge structure factor

$$C_n(k) \equiv \frac{1}{N} \sum_i e^{-ik \cdot r_{0i}} (\langle \hat{n}_i \hat{n}_0 \rangle - \langle \hat{n}_i \rangle \langle \hat{n}_0 \rangle), \quad (\text{S3})$$

is found to peak at $M \equiv (0, \pm \frac{2\pi}{\sqrt{3}})$ point in the Brillouin zone (BZ). Note there are three pairs of equivalent M points in the BZ while only one of them is preferred by the cylindrical geometry, c.f., Ref. [1]. As shown in Fig. S5(b), for the low- T CDW state, the CDW order parameter $C_n(M)$, structure factor at the M point, experiences a sudden drop at the transition temperature $T_c \simeq 0.022$ upon heating, the same temperature as the specific heat peak locates in Fig. S5(a). Again, the mean-field results overestimate T_c , which is believed to be corrected by the higher-order perturbative calculation towards the XTRG results.

To address the universality class of phase transitions between the CDW phase that breaks Z_2 -type (discrete translational) symmetries to the symmetric phase at higher temperatures, we follow the same line as in the main text for the current-current correlation C_J , and perform the finite-size data collapsing of $C_n(M)$ in Fig. S5(c). As a function of t ($\equiv \frac{T-T_c}{T_c}$) and system size L , we denote it as $C_n(M; t, L)$. We again using the 2D Ising critical exponents $\beta = 1/8$ and $\nu = 1$ as the CDW phase breaks Z_2 symmetry. In the inset of Fig. S5(c), we plotted the $C_n(M; t, L)L^{2\beta/L}$ versus T and identify the critical temperature $T_c \simeq 0.024$ as the crossing points between curves of different system sizes. The so-estimated T_c is again very closed to the peak of specific heat. Then we rescale the x -axes of Fig. S5(c) as $tL^{1/\nu}$ and see perfect data collapses within the critical regimes in the main panel of Fig. S5(c).

In Fig. S5(d), we see that the g_2^{nh} correlation increases rapidly as the long-range anti-bunching correlation melts at the CDW transition temperature. Other than that, we also observe similar particle-hole correlation modulation in the exciton-proliferated intermediate- T regime above the CDW phase, as in Fig. 3(d) of the main text. In Fig. S5(d), we also perform the calculation on the compressibility $\partial n/\partial \mu$ by adding a chemical potential term to the KV model. Similarly, the compressibility exhibits a steep jump above T_c and keeps an enhanced value inside the exciton regime.

Section V: Detailed α -scan for phase diagram

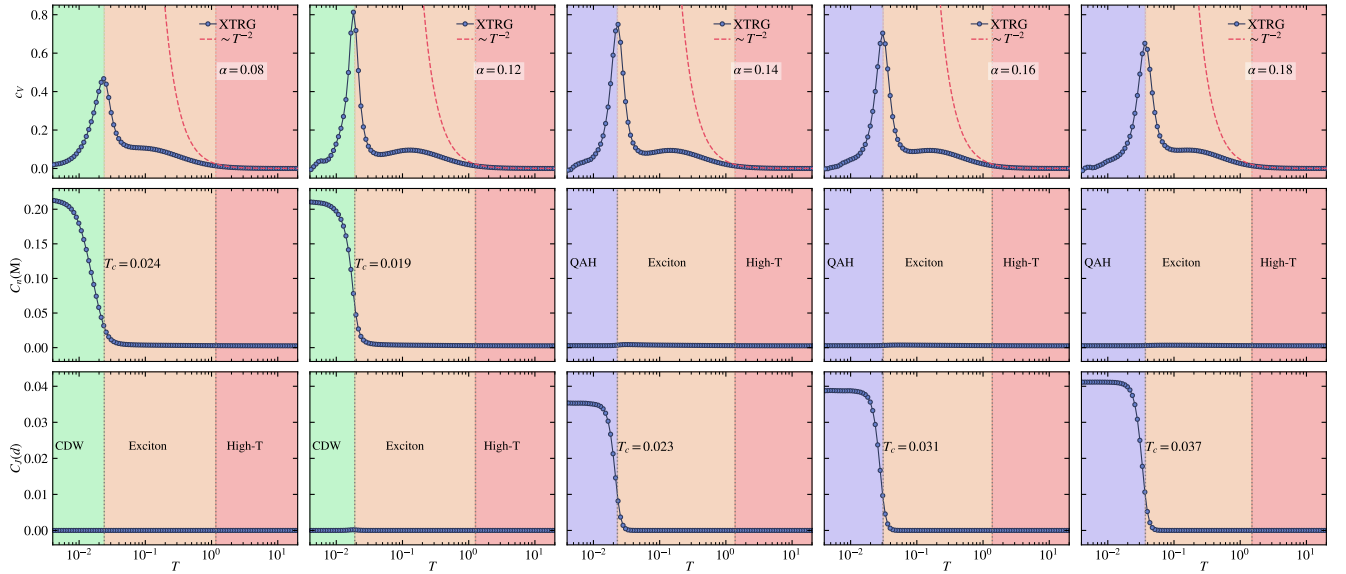


FIG. S6. In a $YC4 \times 12$ system for various $\alpha = 0.08, 0.12, 0.14, 0.16, 0.18$, the specific heat c_V (the first row), the charge density structure factor $C_n(M)$ (the second row), and the current-current correlation $C_J(d=6)$ (the last row), are shown versus temperature T .

In this section, we will show more results of specific heat c_V , charge structure factor $C_n(M)$, and the current-current correlation function $C_J(d=6)$ for various α other than $\alpha = 0.1$ and 0.2 , as complement to the main text. As shown in Fig. S6, in all these cases ($\alpha = 0.08, 0.12, 0.14, 0.16, 0.18$) the specific heat c_V curves (the first row) clearly show sharp peaks, above which either $C_n(M)$ ($\alpha = 0.08$ and 0.12) and $C_J(d=6)$ ($\alpha = 0.14, 0.16$ and 0.18) quickly vanish.

Section VI: Electronic compressibility calculations

In this section, we add a chemical potential term to the original Kang-Vafek model [Eq. (1) in the main text], i.e.

$$H = U_0 \sum_{\square} (Q_{\square} + \alpha T_{\square} - 1)^2 - \mu \sum_i \hat{n}_i, \quad (\text{S4})$$

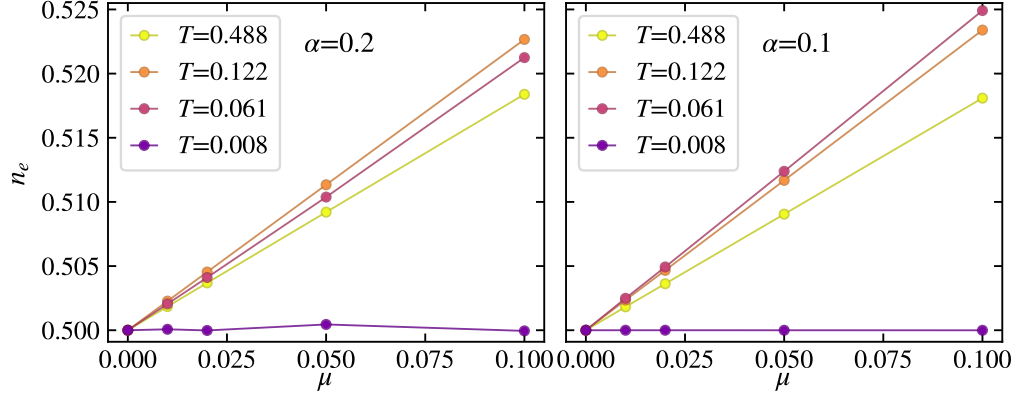


FIG. S7. The averaged charge density n_e as a function of chemical potential μ at various temperatures in the cases of $\alpha = 0.2$ (Left panel) and $\alpha = 0.1$ (Right panel).

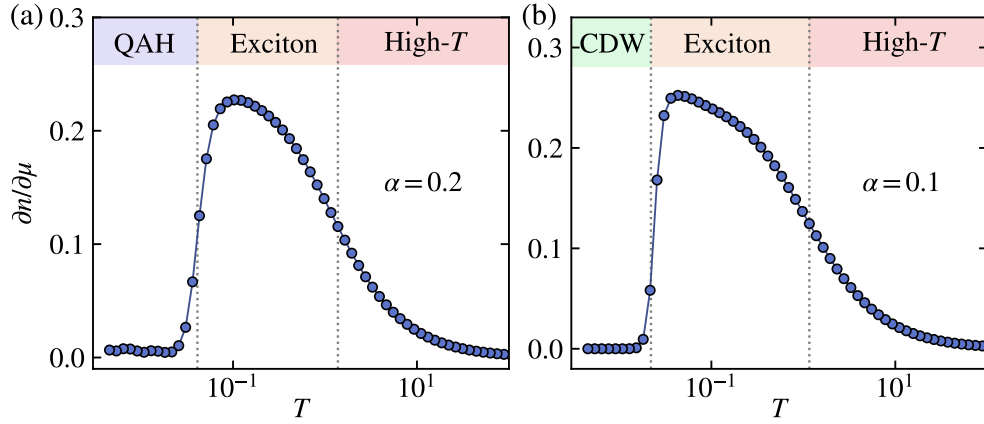


FIG. S8. The temperature-dependent electron compressibility $\partial n/\partial\mu$ of Kang-Vafeek model in the cases of (a) $\alpha = 0.2$, (b) $\alpha = 0.1$. They are duplicates of Fig.3(c) and Fig.S5(c) to keep the present section self-consistent.

to account for the electronic response with chemical potential. We calculate the averaged electron density

$$n_e(\mu, \beta) = \frac{N_e}{N} = \frac{1}{N} \frac{\text{Tr}[\sum_i \hat{n}_i e^{-\beta H(\mu)}]}{\text{Tr}[e^{-\beta H(\mu)}]},$$

for different inverse temperature $\beta = 1/T$ and different chemical potentials μ ranging from 0 to 0.1. As shown in Fig. S7, for both $\alpha = 0.1$ and $\alpha = 0.2$, the particle density responds to chemical potential linearly above the transition temperature. The electronic compressibility at $\mu = 0$ is then approximately obtained via,

$$\frac{\partial n}{\partial \mu} \approx \frac{n_e(\Delta\mu, \beta) - n_e(0, \beta)}{\Delta\mu},$$

where $\Delta\mu = 0.01$ is taken. The obtained compressibility versus temperature is shown in Fig. S8 for two cases of $\alpha = 0.2$ and $\alpha = 0.1$. The results exhibit zero-value compressibility in both QAH and CDW low- T phases due to their insulator nature, whereas show finite-value in the intermediate- T regime verifying the metallic nature.

Section VII: Gaussian state approach to twisted bilayer graphene

At finite temperature T , the imaginary time evolution equation [76] for density matrices ρ reads

$$d_\tau \rho = -\{F(\rho) - f(\rho), \rho\}, \quad (\text{S5})$$

which guarantees the monotonic decrease of the free energy $f(\rho) = \text{tr}(\rho F(\rho))$ with $F(\rho) = H + T \ln \rho$ being the free energy operator.

We approximate the density matrix ρ by the Gaussian state

$$\rho_G = \frac{1}{Z} e^{-\frac{1}{2T} C^\dagger \Omega C}, \quad (\text{S6})$$

where $Z = \text{tr}(e^{-\frac{1}{2T} C^\dagger \Omega C})$ is the partition function, $\Omega = \Omega^\dagger$ is a matrix in the Nambu basis $C^\dagger = (c_1^\dagger, \dots, c_{N_f}^\dagger, c_1, \dots, c_{N_f})$, the creation and annihilation operators c_i^\dagger and c_i fulfill the anti-commutation relation $\{c_i, c_j^\dagger\} = \delta_{ij}$, and N_f is the number of fermionic modes. The density matrix ρ_G is fully characterized by its $2N_f \times 2N_f$ covariance matrix

$$\Gamma = \text{tr}(\rho_G C C^\dagger) = \frac{1}{e^{-\frac{\Omega}{T}} + 1}. \quad (\text{S7})$$

By projecting Eq. (S5) in the tangential space of the variational manifold [75, 76], we obtain EOM

$$\partial_\tau \Gamma = \{\mathcal{F}, \Gamma\} - 2\Gamma \mathcal{F} \Gamma, \quad (\text{S8})$$

where the mean-field free energy $\mathcal{F} = \mathcal{H} - \Omega$ is determined by the mean-field Hamiltonian $\mathcal{H}_{ij} = -2\delta\langle H \rangle_G / \delta\Gamma_{ij}$ and $\langle H \rangle_G = \text{tr}(H \rho_G)$.

For the Kang-Vafek (KV) model Eq. (1), the diagonal and off-diagonal blocks

$$\begin{aligned} \varepsilon &= -M^2 + 2[1 - \text{tr}(\langle cc^\dagger \rangle_G M)]M + 2M \langle cc^\dagger \rangle_G M, \\ \Delta &= -2M \langle cc \rangle_G M, \end{aligned} \quad (\text{S9})$$

of the mean-field Hamiltonian $\mathcal{H} = \begin{pmatrix} \varepsilon & \Delta \\ \Delta^\dagger & -\varepsilon^T \end{pmatrix}$ in the local basis c_i of each hexagon are determined by

$$M = \frac{1}{3} I_6 + \begin{pmatrix} 0 & t_{ab} \\ t_{ab}^\dagger & 0 \end{pmatrix}, t_{ab} = \alpha \begin{pmatrix} -1 & 0 & 1 \\ 1 & -1 & 0 \\ 0 & 1 & -1 \end{pmatrix}. \quad (\text{S10})$$

where the six sites in the hexagon are labeled in Fig. S9. The energy per hexagon reads

$$\langle H_{\square} \rangle_G = [\text{tr}((1 - \langle cc^\dagger \rangle_G) M) - 1]^2 + \text{tr}[(1 - \langle cc^\dagger \rangle_G) M \langle cc^\dagger \rangle_G M] + \text{tr}[M \langle c^\dagger c \rangle_G M \langle cc \rangle_G]. \quad (\text{S11})$$

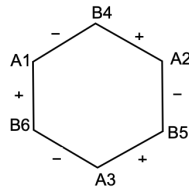


FIG. S9. The labels of the six sites in the hexagon.

The free energy

$$f(\rho) = \sum_{\square} \langle H_{\square} \rangle_G - \frac{1}{2} \text{tr}[(1 - \Gamma)\Omega + T \ln(e^{-\frac{\Omega}{T}} + 1)] \quad (\text{S12})$$

decreases monotonically in the imaginary time evolution, where the diagonal matrix $E = \text{diag}(E_1, E_2, \dots, E_{2N_f})$ is constructed by the eigenvalues of Ω . In the asymptotic limit, the density matrix reaches the thermal equilibrium state, where $\mathcal{H} = \Omega$, and the pairing term $\langle c_i c_j \rangle_G = \langle c_i^\dagger c_j^\dagger \rangle_G = 0$ due to the repulsive Coulomb interaction inherited by the KV model. As a result, the off-diagonal block $\Delta = 0$.

In agreement with the XTRG approach, the finite-T phase diagram obtained by the optimal mean-field theory consists of the QAH states, the CDW states, and high-T trivial states. It is remarkable that the QAH and CDW states possess a lot of symmetries

which are represented by the structure of the covariance matrix Γ . Therefore, the thermal state can be described with very little order parameters, as we will show in the following.

Let us list several typical symmetries S of the Hamiltonian. The Hamiltonian has the particle hole symmetry S_c , the time reversal symmetry S_T , the translational symmetry $P_{\vec{a}_j}$ ($j = 1, 2, 3$), the rotational symmetry R_3 with respect to the center of the hexagon, the reflection symmetry Z_{2h} with respect to the horizontal axis x_1 , the symmetry $n_A Z_{2v}$ of the reflection with respect to the vertical axis x_2 and $c_i \rightarrow -c_i$ in one sub-lattice. The vectors and axes in the honeycomb Moiré lattice are shown in Fig. S10.

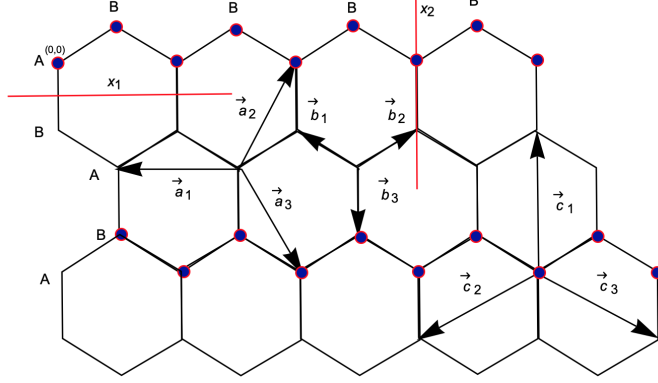


FIG. S10. The horizontal and vertical axis x_1 and x_2 . The sublattice A of the honeycomb lattice are generated by linear combinations of the basis vectors $\vec{a}_1 = (-\sqrt{3}, 0)$, $\vec{a}_2 = \left(\frac{\sqrt{3}}{2}, \frac{3}{2}\right)$, $\vec{A}(n_1 n_2) = n_1 \vec{a}_1 + n_2 \vec{a}_2$, where n_1, n_2 are intergers. The sublattices A and B are connected by the vectors $\vec{b}_1 = \left(\frac{-\sqrt{3}}{2}, \frac{1}{2}\right)$, $\vec{b}_2 = \left(\frac{\sqrt{3}}{2}, \frac{1}{2}\right)$, $\vec{b}_3 = (0, -1)$. And here are other uesful vectors $\vec{a}_3 = \left(\frac{\sqrt{3}}{2}, -\frac{3}{2}\right)$, $\vec{c}_1 = (0, 2)$, $\vec{c}_2 = (-\sqrt{3}, -1)$, $\vec{c}_3 = (\sqrt{3}, -1)$.

The covariance matrix $\gamma = \langle cc^\dagger \rangle_G$ in the coordinate space shows that the QAH state has symmetries S_c , $P_{\vec{a}_j}$ ($j = 1, 2, 3$), R_3 and the symmetry $S_T Z_{2h}$. The properties of γ and the corresponding symmetry are listed as follows:

- The particle-hole symmetry $S_c \implies \gamma = 1 - \gamma^T \xrightarrow{\gamma = \gamma^\dagger} \gamma_{ii} = 0.5, \text{Re}(\gamma_{ij(i \neq j)}) = 0$.
- The translational symmetry $P_{\vec{a}_j}$ ($j = 1, 2, 3$) \implies The covariance matrices for all hexagons are same, e.g., $\gamma_{41} = \gamma_{53}$.
- The rotational symmetry $R_3 \implies \gamma_{41} = \gamma_{63} = \gamma_{52}, \gamma_{53} = \gamma_{42} = \gamma_{61}, \gamma_{21} = \gamma_{13} = \gamma_{32}, \gamma_{54} = \gamma_{46} = \gamma_{65}, \gamma_{43} = \gamma_{62} = \gamma_{51}$.
- The symmetry $S_T Z_{2h} \implies \gamma_{23} = \gamma_{54}^*$.

The symmetries play an important role since they completely determine the covariance matrix

$$\langle cc^\dagger \rangle_G = \gamma = \begin{pmatrix} \gamma_a & \gamma_{ab} \\ \gamma_{ab}^\dagger & \gamma_a \end{pmatrix}, \gamma_a = \begin{pmatrix} 0.5 & \delta^* & \delta \\ \delta & 0.5 & \delta^* \\ \delta^* & \delta & 0.5 \end{pmatrix}, \gamma_{ab} = \begin{pmatrix} \delta_{ab} & \delta_{ab2} & \delta_{ab} \\ \delta_{ab} & \delta_{ab} & \delta_{ab2} \\ \delta_{ab2} & \delta_{ab} & \delta_{ab} \end{pmatrix} \quad (\text{S13})$$

with only three independent order parameters

$$\begin{aligned} \delta_{ab} &= \langle b_{\vec{A}+\vec{b}_j}^\dagger a_{\vec{A}} \rangle_G, \\ \delta &= \langle a_{\vec{A}+\vec{a}_j}^\dagger a_{\vec{A}} \rangle_G = \langle b_{\vec{A}+\vec{b}_1+\vec{a}_j}^\dagger b_{\vec{A}+\vec{b}_1} \rangle_G, \\ \delta_{ab2} &= \langle b_{\vec{A}+\vec{c}_j}^\dagger a_{\vec{A}} \rangle_G, \quad j = 1, 2, 3, \end{aligned} \quad (\text{S14})$$

where $a_{\vec{r}_a}$ and $b_{\vec{r}_b}$ are the annihilation operators of electrons in sublattices A and B .

The covariance matrix gives rise to the mean-field Hamiltonian

$$\varepsilon = \begin{pmatrix} T_a & T_{ab} \\ T_{ab}^\dagger & T_a \end{pmatrix}, T_a = \begin{pmatrix} 0 & t_2 & t_2^* \\ t_2^* & 0 & t_2 \\ t_2 & t_2^* & 0 \end{pmatrix}, T_{ab} = \begin{pmatrix} \bar{t}_1^* & t_3^* & \bar{t}_1^* \\ \bar{t}_1^* & \bar{t}_1^* & t_3^* \\ t_3^* & \bar{t}_1^* & \bar{t}_1^* \end{pmatrix} \quad (\text{S15})$$

in each hexagon through Eq. (S9), with the effective hopping strengths

$$\begin{aligned} \bar{t}_1 &= 2 \left(\alpha^2 + \frac{1}{9} \right) \delta_{ab} - \frac{4}{3} \alpha \delta - 2\alpha^2 \delta_{ab2}, \\ t_2 &= 2 \left(-\frac{2\alpha\delta_{ab}}{3} + \left(3\alpha^2 + \frac{1}{9} \right) \delta + \frac{2\alpha\delta_{ab2}}{3} \right), \\ t_3 &= 2 \left(-2\alpha^2 \delta_{ab} + \frac{4\alpha\delta}{3} + \left(2\alpha^2 + \frac{1}{9} \right) \delta_{ab2} \right). \end{aligned} \quad (\text{S16})$$

between the nearest neighbor, the second-neighbor, and the third-neighbor sites, as shown in Fig. S11.

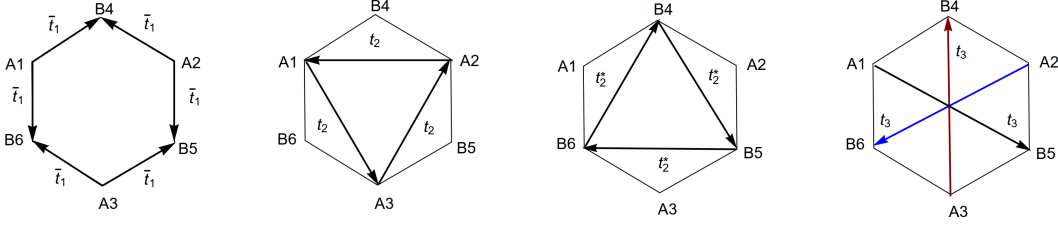


FIG. S11. The effective hopping strengths of the mean field Hamiltonian in QAH phases.

In the second quantized form, the mean-field Hamiltonian of the honeycomb Moiré lattice reads

$$H = \sum_{\vec{A}} \sum_j \left[t_1 b_{A+\vec{b}_j}^\dagger a_{\vec{A}} + t_2 a_{A+\vec{a}_j}^\dagger a_{\vec{A}} + t_2^* b_{A+\vec{b}_1+\vec{a}_j}^\dagger b_{A+\vec{b}_1} + t_3 b_{A+\vec{c}_j}^\dagger a_{\vec{A}} + h.c. \right], \quad (\text{S17})$$

where $t_1 = 2\bar{t}_1$. The Fourier transforms $a_k = \sum_{\vec{A}} e^{-i\vec{k}\cdot\vec{A}} a_{\vec{A}} / \sqrt{N}$ and $b_k = \sum_{\vec{A}} e^{-i\vec{k}\cdot(\vec{A}+\vec{b}_j)} b_{\vec{A}+\vec{b}_j} / \sqrt{N}$ result in the mean-field Hamiltonian $H = \sum_{\vec{k}} c_k^\dagger h^{\text{QAH}}(k) c_k$ in the momentum space $c_k = (a_k, b_k)^T$, where

$$h^{\text{QAH}}(k) = \begin{pmatrix} h_{k,11} & h_{k,12} \\ h_{k,12}^* & -h_{k,11} \end{pmatrix} \quad (\text{S18})$$

is determined by

$$\begin{aligned} h_{k,11} &= t_2 \sum_j e^{-i\vec{k}\cdot\vec{a}_j} + t_2^* \sum_j e^{i\vec{k}\cdot\vec{a}_j}, \\ h_{k,12} &= t_1^* \sum_j e^{i\vec{k}\cdot\vec{b}_j} + t_3 \sum_j e^{i\vec{k}\cdot\vec{c}_j}. \end{aligned} \quad (\text{S19})$$

The covariance matrix

$$\left\langle c_k c_k^\dagger \right\rangle_{\text{G}} = \frac{1}{e^{-\frac{1}{T} h^{\text{QAH}}(k)} + 1} = \frac{h^{\text{QAH}}(k)}{2d_{k,c}} (1 - 2f_k^c) + \frac{1}{2} I_2 \quad (\text{S20})$$

can be obtained by the diagonalization $U_k^\dagger h^{\text{QAH}}(k) U_k = \text{diag}(d_{k,c}, d_{k,v})$ of the mean-field Hamiltonian $h^{\text{QAH}}(k)$ using the unitary transformation U_k , where the Fermi-Dirac distribution $f_k^\beta = 1/(e^{d_{k,\beta}/T} + 1)$ is determined by the dispersion relations $d_{k,(c,v)} = \pm \sqrt{h_{k,11}^2 + |h_{k,12}|^2}$ in the conduction (v) and valance (v) bands at the temperature T .

The covariance matrix gives rise to the self-consistent equations

$$\begin{aligned} \delta_{ab} &= \frac{1}{2N} \sum_k e^{-i\vec{k}\cdot\vec{b}_j} \frac{-h_{12}}{d_{k,c}} \tanh\left(\frac{d_{k,c}}{2T}\right), \\ \delta &= \frac{1}{2N} \sum_k e^{-i\vec{k}\cdot\vec{a}_j} \frac{-h_{11}}{d_{k,c}} \tanh\left(\frac{d_{k,c}}{2T}\right), \\ \delta_{ab2} &= \frac{1}{2N} \sum_k e^{-i\vec{k}\cdot\vec{c}_j} \frac{-h_{12}}{d_{k,c}} \tanh\left(\frac{d_{k,c}}{2T}\right) \end{aligned} \quad (\text{S21})$$

for the order parameters. Close to the phase transition, all the order parameters tend to zero, and Eq. (S21) can be linearized as

$$\begin{pmatrix} \delta_{ab} \\ \delta \\ \delta_{ab2} \end{pmatrix} = \frac{1}{4T} \begin{pmatrix} t_1 \\ t_2 \\ t_3 \end{pmatrix} = \frac{1}{T} M_{\text{QAH}} \begin{pmatrix} \delta_{ab} \\ \delta \\ \delta_{ab2} \end{pmatrix}. \quad (\text{S22})$$

The critical temperature T_c is thus determined by the largest positive eigenvalue λ_{max} of

$$M_{\text{QAH}} = \frac{1}{2} \begin{pmatrix} 2\alpha^2 + \frac{2}{9} & -\frac{4}{3}\alpha & -2\alpha^2 \\ -\frac{2}{3}\alpha & 3\alpha^2 + \frac{1}{9} & \frac{2}{3}\alpha \\ -2\alpha^2 & \frac{4}{3}\alpha & 2\alpha^2 + \frac{1}{9} \end{pmatrix}.$$

Furthermore, using symmetries we can significantly reduce the degrees of freedom in the $N_f \times N_f$ covariance matrix to three order parameters, as a result, the above analysis can be applied to the system in the thermodynamic limit. To speed up the calculation, we first numerically solve the flow equations of γ for a small system, and achieve the three order parameters in the thermal state. Using the order parameters of the small system as the initial condition, we solve the non-linear Eq. (S21) to obtain the order parameters for the system in the thermodynamic limit, where the free energy density

$$f(\delta_{ab}, \delta, \delta_{ab2}) = \langle H_{\text{O}} \rangle_{\text{G}} + \frac{1}{N_f} \sum_k 2T [f_k^c \ln f_k^c + f_k^v \ln f_k^v] \quad (\text{S23})$$

is minimized.

In the CDW phase, the density distribution of the CDW state has three equivalent spatial structures for the system in the thermodynamic limit, which possesses the symmetries $P_{\vec{a}_1}$, $P_{\vec{a}_2}$ and $P_{\vec{a}_3}$, respectively. We analyze one of the three equivalent CDW states that maintains the symmetry $P_{\vec{a}_1}$ without loss of generality. The structure of the covariance matrices $\gamma_{\text{odd}} \equiv \lambda$ and γ_{even} in the odd and even rows, respectively, indicates that the CDW state possesses the symmetries S_T , $P_{\vec{a}_1}$, $n_A Z_{2v}$, and the combination symmetries $S_c P_{\vec{a}_3}$, $S_c Z_{2h}$. The properties of the covariance matrices and the corresponding symmetry are listed as follows.

- The time reversal symmetry $S_T \implies \lambda = \lambda^* \xrightarrow{\lambda=\lambda^\dagger} \gamma_{\text{odd}}$ and γ_{even} are real symmetric matrices.
- The translational symmetry $P_{\vec{a}_1} \implies$ The covariance matrices for each rows are same, e.g., $\lambda_{11} = \lambda_{22}$.
- The combination symmetry $S_c P_{\vec{a}_3} \implies \gamma_{\text{odd}} = I - \gamma_{\text{even}}^T$, $\lambda_{14} = -\lambda_{35}$, $\lambda_{44} = 1 - \lambda_{55}$.
- The combination symmetry $S_c Z_{2h} \implies \lambda_{11} = 1 - \lambda_{66}$, $\lambda_{22} = 1 - \lambda_{55}$, $\lambda_{44} = 1 - \lambda_{33}$; $\lambda_{16} = \lambda_{25} = 0$, $\lambda_{14} = -\lambda_{63}$, $\lambda_{24} = -\lambda_{53}$; $\lambda_{12} = -\lambda_{56}$, $\lambda_{13} = -\lambda_{64}$, $\lambda_{23} = -\lambda_{54}$; $\lambda_{15} = -\lambda_{62}$, $\lambda_{34} = -\lambda_{43} = 0$.
- The symmetry $n_A Z_{2v} \implies \lambda_{13} = \lambda_{23}$, $\lambda_{36} = -\lambda_{35}$.

Therefore, the covariance matrix γ only has four independent order parameters

$$\begin{aligned} n_0 &= \langle a_{\vec{A}_o} a_{\vec{A}_o}^\dagger \rangle_{\text{G}} - \frac{1}{2}, \\ n_1 &= \langle a_{\vec{A}_o} a_{\vec{A}_o - \vec{a}_1}^\dagger \rangle_{\text{G}}, \\ n_2 &= \langle a_{\vec{A}_o} a_{\vec{A}_o + \vec{a}_3}^\dagger \rangle_{\text{G}}, \\ \Delta_0 &= \langle a_{\vec{A}_o} b_{\vec{A}_o + \vec{c}_2}^\dagger \rangle_{\text{G}}, \end{aligned} \quad (\text{S24})$$

where $\vec{A}_o = l_1 \vec{a}_1 + 2l_2 \vec{a}_3$ and $l_{1,2}$ are integers. The covariance matrix

$$\gamma_{\text{odd}} = \begin{pmatrix} n_0 + \frac{1}{2} & n_1 & n_2 & 0 & -\Delta_0 & 0 \\ n_1 & n_0 + \frac{1}{2} & n_2 & 0 & 0 & \Delta_0 \\ n_2 & n_2 & \frac{1}{2} - n_0 & 0 & 0 & 0 \\ 0 & 0 & 0 & n_0 + \frac{1}{2} & -n_2 & -n_2 \\ -\Delta_0 & 0 & 0 & -n_2 & \frac{1}{2} - n_0 & -n_1 \\ 0 & \Delta_0 & 0 & -n_2 & -n_1 & \frac{1}{2} - n_0 \end{pmatrix} \quad (\text{S25})$$

results in the mean-field Hamiltonian

$$\varepsilon^o = \begin{pmatrix} e_1 & e_3 & e_4 & e_5 & e_6 & 0 \\ e_3 & e_1 & e_4 & -e_5 & 0 & -e_6 \\ e_4 & e_4 & e_2 & 0 & e_5 & -e_5 \\ e_5 & -e_5 & 0 & -e_2 & -e_4 & -e_4 \\ e_6 & 0 & e_5 & -e_4 & -e_1 & -e_3 \\ 0 & -e_6 & -e_5 & -e_4 & -e_3 & -e_1 \end{pmatrix} \quad (\text{S26})$$

in odd rows with the hopping strengths

$$\begin{aligned} e_1 &= \frac{2}{9}n_0 + 4\alpha^2 n_2, \\ e_2 &= -\frac{2}{9}n_0 + 2\alpha^2(-2n_0 + 2n_1), \\ e_3 &= \frac{2}{9}n_1 + \frac{4\alpha}{3}\Delta_0 + \alpha^2(-2n_0 + 2n_1 - 4n_2), \\ e_4 &= \frac{2}{9}n_2 - \frac{2\alpha}{3}\Delta_0 - \alpha^2(-2n_0 + 2n_1), \\ e_5 &= -\frac{2}{3}\alpha(2n_0 - n_1 + n_2 - 3\alpha\Delta_0), \\ e_6 &= \frac{2}{9}(6\alpha(n_2 - n_1) - (1 + 9\alpha^2)\Delta_0). \end{aligned} \quad (\text{S27})$$

The combination symmetry $S_c P_{\vec{a}_3}$ determines the relation between the mean-field Hamiltonian in odd and even rows as $\varepsilon^o = -\varepsilon^e$.

In the second quantized form, the mean-field Hamiltonian of the honeycomb Moiré lattice reads

$$H = \sum_{\square^o} \sum_{i,j \in \square^o} c_i^\dagger \varepsilon_{i,j}^o c_j + \sum_{\square^e} \sum_{i,j \in \square^e} c_i^\dagger \varepsilon_{i,j}^e c_j. \quad (\text{S28})$$

The stripe has the translational symmetry $P_{\vec{a}_1}$ and $P_{2\vec{a}_3}$, thus, particles with the momentum $k_h \in \{[0, 2\pi_x/\sqrt{3}], [0, 2\pi_y/3]\}$ hybridize with particles with the momentum $k_{h\pm} = k_h \pm 2\pi_y/3$ and the Brillouin zone shrinks to $k_h \in \{[0, 2\pi_x/\sqrt{3}], [0, 2\pi_y/3]\}$, which is different from the situation in QAH phases. The Fourier transformation gives rise to the mean-field Hamiltonian $H = \sum_{k_h} c_{k_h}^\dagger h^{\text{CDW}}(k_h) c_{k_h}$ in the momentum space $c_{k_h} = (a_{k_h}, b_{k_h}, a_{k_{h\pm}}, b_{k_{h\pm}})$, where

$$h^{\text{CDW}}(k_h) = \begin{pmatrix} 0 & \bar{h}_0^\dagger(k_h) \\ \bar{h}_0(k_h) & 0 \end{pmatrix} \quad (\text{S29})$$

is determined by

$$\bar{h}_0(k_h) = \begin{pmatrix} \varepsilon_{k_h} & \bar{\varepsilon}_{k_h} \\ -e^{-i\frac{\pi}{3}} \varepsilon_{k_h}^* & e^{-i\frac{\pi}{3}} \varepsilon_{k_h}^* \end{pmatrix}, \quad (\text{S30})$$

and

$$\begin{aligned} \varepsilon_k &= 2e_1 - e_2 + 2e_3 \cos(\sqrt{3}k_x) - 4ie_4 \cos\left(\frac{\sqrt{3}}{2}k_x\right) \sin\left(\frac{3}{2}k_y\right), \\ \bar{\varepsilon}_k &= 2ie^{-ik_y} e_6 \sin(\sqrt{3}k_x). \end{aligned} \quad (\text{S31})$$

The covariance matrix

$$\left\langle \left(\begin{array}{c} c_k \\ c_{k'} \end{array} \right) \left(\begin{array}{cc} c_k^\dagger & c_{k'}^\dagger \end{array} \right) \right\rangle_{\text{G}} = \frac{1}{e^{-\frac{1}{T}h^{\text{CDW}}(k)} + 1} = \begin{pmatrix} \frac{1}{2} & \frac{1}{2E_k} \bar{h}_0^\dagger(k) (1 - 2f_k) \\ \frac{1}{2E_k} \bar{h}_0(k) (1 - 2f_k) & \frac{1}{2} \end{pmatrix} \quad (\text{S32})$$

can be obtained by the diagonalization $U_k^\dagger h^{\text{CDW}}(k) U_k = \text{diag}(E_k, E_k, -E_k, -E_k)$ of the mean-field Hamiltonian $h^{\text{CDW}}(k)$ using the unitary transformation U_k , where the Fermi-Dirac distribution in the CDW phase $f_k = 1/(e^{E_k/T} + 1)$ is determined by the dispersion relation $E_k = \sqrt{|\varepsilon_k|^2 + |\bar{\varepsilon}_k|^2}$ at the temperature T .

The covariance matrix leads to the self-consistent equations

$$\begin{aligned}
n_0 &= \frac{1}{N} \sum_k \frac{\varepsilon_k}{2E_k} \tanh\left(\frac{E_k}{2T}\right), \\
n_1 &= \frac{1}{N} \sum_k e^{ik\vec{a}_1} \frac{\varepsilon_k}{2E_k} \tanh\left(\frac{E_k}{2T}\right), \\
n_2 &= \frac{1}{N} \sum_k e^{-ik\vec{a}_3} \frac{\varepsilon_k}{2E_k} \tanh\left(\frac{E_k}{2T}\right), \\
\delta_0 &= \frac{1}{N} \sum_k e^{-ik\vec{c}_3} \frac{-\bar{\varepsilon}_k}{2E_k} \tanh\left(\frac{E_k}{2T}\right)
\end{aligned} \tag{S33}$$

for the order parameters. Close to the phase transition, all the order parameters tend to zero, and Eq. (S33) can be linearized as

$$\begin{aligned}
4Tn_0 &= 2e_1 - e_2 = \left(\frac{2}{3} + 4\alpha^2\right)n_0 - 4\alpha^2n_1 + 8\alpha^2n_2, \\
4Tn_1 &= e_3 = -2\alpha^2n_0 + \left(\frac{2}{9} + 2\alpha^2\right)n_1 - 4\alpha^2n_2 - \frac{4\alpha}{3}\delta_0, \\
4Tn_2 &= e_4 = 2\alpha^2n_0 - 2\alpha^2n_1 + \frac{2}{9}n_2 + \frac{2\alpha}{3}\delta_0, \\
4T\delta_0 &= e_6 = \frac{2}{9}[-6\alpha n_1 + 6\alpha n_2 + (1 + 9\alpha^2)\delta_0].
\end{aligned} \tag{S34}$$

The critical temperature $T_c = \lambda_{\max}/4$ is determined by the largest positive eigenvalue λ_{\max} of the matrix

$$M_{\text{CDW}} = \begin{pmatrix} \frac{2}{3} + 4\alpha^2 & -4\alpha^2 & 8\alpha^2 & 0 \\ -2\alpha^2 & \frac{2}{9} + 2\alpha^2 & -4\alpha^2 & -\frac{4}{3}\alpha \\ 2\alpha^2 & -2\alpha^2 & \frac{2}{9} & \frac{2}{3}\alpha \\ 0 & -\frac{4}{3}\alpha & \frac{4}{3}\alpha & \frac{2}{9} + 2\alpha^2 \end{pmatrix}. \tag{S35}$$

Finally, the finite-T phase diagram S12 under the self-consistent mean-field approximation can be obtained, where the first-order transition between the QAH and CDW phases is displayed.

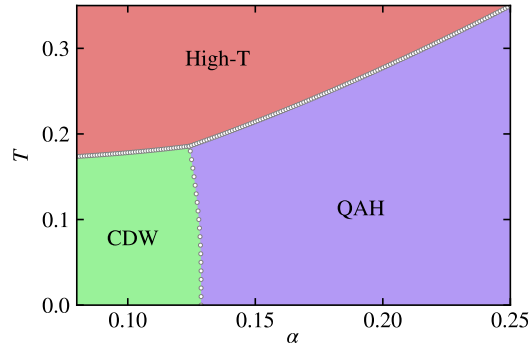


FIG. S12. The finite-T phase diagram obtained by the Gaussian state theory.

Section VIII: Exciton spectra and self-energy corrections

At zero temperature, the single-particle Green's function from the Gaussian state approach (the self-consistent mean-field theory) agrees excellently with the result from DMRG [1]. With respect to the Gaussian thermal state ρ_G described by three

order parameters in QAH phases, the KV Hamiltonian (S36) is decomposed into normal ordered terms via the Wick theorem as

$$\begin{aligned} H &= \langle H \rangle + \sum_{\square} :c_i^\dagger M_{ij} c_j: + \sum_{\square} :c_i^\dagger M_{ij} c_j c_l^\dagger M_{lm} c_m:, \\ &= \langle H \rangle + \sum_k :c_{k,\alpha}^\dagger h_{\alpha\beta}^{\text{QAH}}(k) c_{k,\beta}: + \frac{1}{N} \sum_{k,p,q} (V_{k-q}^\dagger M V_k)_{\alpha\beta} (V_p^\dagger M V_{p-q})_{\bar{\alpha}\bar{\beta}} :c_{k-q,\alpha}^\dagger c_{k,\beta} c_{p,\bar{\alpha}}^\dagger c_{p-q,\bar{\beta}}:, \end{aligned} \quad (\text{S36})$$

where the Fourier transformation $V_k = \begin{pmatrix} e^{ikr_A^h} & 0 \\ 0 & e^{ikr_B^h} \end{pmatrix}$ is determined by the relative distance $r_A^h = ((0, 0), (\sqrt{3}, 0), (\sqrt{3}/2, -3/2))^T$ and $r_B^h = ((\sqrt{3}/2, 1/2), (\sqrt{3}, -1), (0, -1))^T$, and we use the Einstein summation convention for the Greek alphabet.

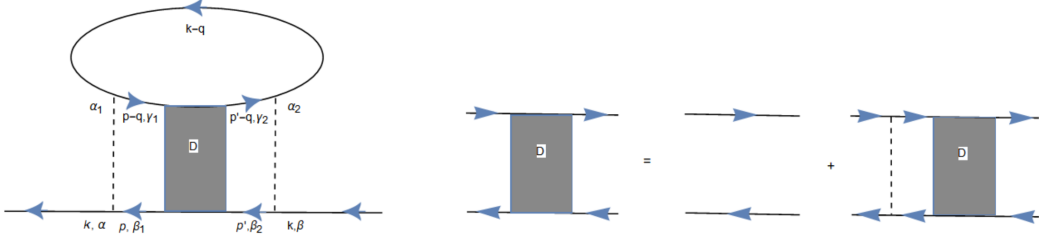


FIG. S13. The Hartree-like self energy $\Sigma_{k,\alpha\beta}^{(H)}$.

At finite temperature, the two-particle spectrum can be obtained by the ladder diagram approximation beyond the mean-field theory, as shown in Fig. S13, and the self-energy correction, e.g., the Hartree term, becomes

$$\begin{aligned} \Sigma_{k,\alpha\beta}^{(H)} &= - \left(\frac{2}{N} \right)^2 \sum_{pp'q} T \sum_{\omega_q} G_{k-q}^{(0)\alpha_1\alpha_2}(\omega_k - \omega_q) (V_k^\dagger M V_p)_{\alpha\beta_1} (V_{p-q}^\dagger M V_{k-q})_{\alpha_1\gamma_1}^T \\ &\quad D_{pp'}^{\beta_1\gamma_1,\beta_2\gamma_2}(q, \omega_q) (V_{k-q}^\dagger M V_{p'-q})_{\gamma_2\alpha_2}^T (V_{p'}^\dagger M V_k)_{\beta_2\beta}, \end{aligned} \quad (\text{S37})$$

where the free single-particle Green function $G_k^{(0)}(\omega_k) = 1/(i\omega_k - h^{\text{QAH}}(k))$. The exciton spectrum can be determined by the density-density correlation function

$$\begin{aligned} D_{pp'}^{\beta_1\gamma_1,\beta_2\gamma_2}(q, \omega_q) &= \int_0^\beta d\tau D_{pp'}^{\beta_1\gamma_1,\beta_2\gamma_2}(q, \tau) e^{i\omega_q\tau}, \\ D_{pp'}^{\beta_1\gamma_1,\beta_2\gamma_2}(q, \tau) &= -\langle T_\tau c_{p-q,\gamma_1}^\dagger(\tau) c_{p,\beta_1}(\tau) c_{p',\beta_2}^\dagger(0) c_{p'-q,\gamma_2}(0) \rangle. \end{aligned} \quad (\text{S38})$$

It follows from the Heisenberg EOM that

$$-\partial_\tau D_{pp'}^{\beta_1\gamma_1,\beta_2\gamma_2}(q, \tau) = (\langle c_{p-q,\gamma_1}^\dagger c_{p-q,\gamma_2} \rangle_G \delta_{\beta_1,\beta_2} - \langle c_{p,\beta_2}^\dagger c_{p,\beta_1} \rangle_G \delta_{\gamma_1,\gamma_2}) \delta_{p,p'} \delta(\tau) + \sum_{k'} \mathcal{M}_{p,k'}^{\beta_1\gamma_1,\beta_2\gamma_2}(q) D_{k'p'}^{\beta_1\gamma_1,\beta_2\gamma_2}(q, \tau), \quad (\text{S39})$$

where

$$\begin{aligned} \mathcal{M}_{p,k'}^{\beta_1\gamma_1,\beta_2\gamma_2}(q) &= (h_{\beta_1\beta}^{\text{QAH}}(p) \delta_{\gamma_1\gamma} - \delta_{\beta_1\beta} h_{\gamma\gamma_1}^{\text{QAH}}(p-q)) \delta_{p,k'} \\ &\quad + \frac{2}{N} [\langle c_{p,\bar{\beta}}^\dagger c_{p,\beta_1} \rangle_G (V_p^\dagger M V_{k'})_{\bar{\beta}\beta} (V_{k'-q}^\dagger M V_{p-q})_{\gamma\gamma_1} \\ &\quad - (V_p^\dagger M V_{k'})_{\beta_1\beta} \langle c_{p-q,\gamma_1}^\dagger c_{p-q,\bar{\gamma}} \rangle_G (V_{k'-q}^\dagger M V_{p-q})_{\gamma\bar{\gamma}}]. \end{aligned} \quad (\text{S40})$$

We define the correlation function $\bar{D}_{pp'}^{\beta_1\gamma_1,\beta_2\gamma_2} \equiv D_{pp'}^{\beta_1\gamma_1,\beta_2\gamma_2} U_{p-q,\gamma_1\gamma_1} U_{p,\beta_1\beta_1}^* U_{p',\beta_2\beta_2} U_{p'-q,\gamma_2\gamma_2}^*$ in the quasi-particle basis using the transformation U_k . The Fourier transform of EOM (S39) results in

$$\bar{D}_{kp}^{\beta_1\gamma_1,\beta_2\gamma_2}(q, \omega_q) = \left[\frac{1}{[\bar{D}^{(0)}(q, \omega_q)]^{-1} - \mathcal{V}(q)} \right]_{k,p}^{\beta_1\gamma_1,\beta_2\gamma_2}, \quad (\text{S41})$$

where the bare density-density correlation function reads

$$\bar{D}_{kp}^{(0)\beta_1\gamma_1,\beta_2\gamma_2}(q,\omega_q) = \frac{f_{k-q}^{\gamma_1} - f_k^{\beta_1}}{i\omega_q - (d_{k,\beta_1} - d_{k-q,\gamma_1})} \delta_{\beta_1\beta_2} \delta_{\gamma_1\gamma_2} \delta_{k,p}, \quad (\text{S42})$$

and the interaction $\mathcal{V}_{k,k'}^{\beta_1\gamma_1,\beta_2\gamma_2}(q) = -2V_{k,k'}^{\beta_1\beta_2} V_{k'-q,k-q}^{\gamma_1\gamma_2}/N$ of two quasi-particles is determined by $V_{k,k'}^{\beta_1\beta_2} = (U_k^\dagger V_k^\dagger M V_{k'} U_{k'})_{\beta_1\beta_2}$. The spectral decomposition results in

$$\bar{D}_{p,p'}^{\beta_1\gamma_1,\beta_2\gamma_2}(q,\omega_q) = \sum_{\lambda} \chi_{p,\lambda}^{\beta_1\gamma_1}(q) \frac{1}{i\omega_q - d_{2,\lambda}(q)} \bar{\chi}_{\lambda,p'}^{\beta_2\gamma_2*}(q), \quad (\text{S43})$$

where the poles $\pm |d_{2,\lambda}(q)|$ of $\bar{D}_{p,p'}^{\beta_1\gamma_1,\beta_2\gamma_2}(q,\omega_q)$ appear in pairs due to the particle-hole symmetry of $[\bar{D}^{(0)}(q,\omega_q)]^{-1} - \mathcal{V}(q)$. It turns out that the lowest band with the dispersion relation $d_{\text{ex}}(q) = \min_{\lambda} |d_{2,\lambda}(q)|$ corresponds to a collective mode, i.e., the exciton excitation. The bottom of the exciton band is at the Γ -point, and at zero temperature its energy is about 0.08 for $\alpha = 0.2$, i.e., one order of magnitude smaller than the bare quasi-particle gap. Additionally, the exciton is robust in the presence of the kinetic energy of the bare electron as illustrated in Fig. S14. The wavefunction of the exciton state in the coordinate space, i.e., the Fourier transformation of $\chi_{p,\lambda}^{\beta_1\gamma_1}(q)$, shows that the exciton with the center-of-mass momentum q is in the bound state of one electron in the conductive band and one electron in the valence band.

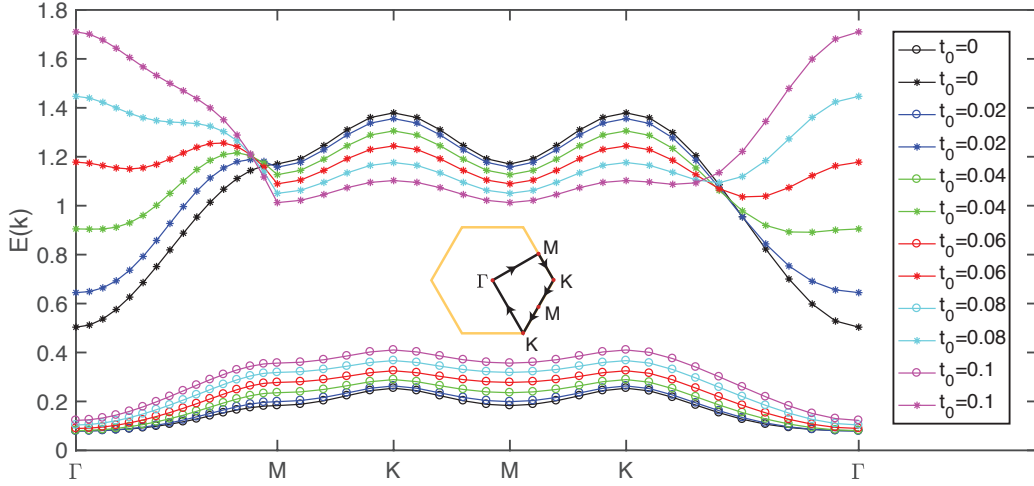


FIG. S14. The bare quasi-particle gap (stars) and the exciton band (circles) obtained via the Hamiltonian $H_{\text{new}} = -t_0 \sum_{\langle i,j \rangle} (c_i^\dagger c_j + h.c.) + U_0 \sum_{\square} (Q_{\square} + \alpha T_{\square} - 1)^2$ at the effective kinetic strength $t_0 = 0, 0.02, 0.04, 0.06, 0.08$ and 0.1 , where $\alpha = 0.2$, the interaction strength $U_0 = 1$ and the temperature $T = 0.04$. The exciton energy is always one order of magnitude smaller than the mean-field gap in the presence of the kinetic energy.

The two-particle correlation function leads to the self-energy correction $\Sigma_k^{(H)} = U_k \bar{\Sigma}_k^{(H)} U_k^\dagger$ via Eq. (S37), where $\bar{\Sigma}_k^{(H)}$ is the self-energy

$$\bar{\Sigma}_{k,\alpha\beta}^{(H)} = \frac{4}{N^2} \sum_{pp'q} \frac{1 - f_{k-q}^{\alpha'} + n_b(d_{2,\lambda}(q))}{i\omega_k - d_{k-q,\alpha'} - d_{2,\lambda}(q)} V_{k,p}^{\alpha\beta_1} V_{p-q,k-q}^{\gamma_1\alpha'} \chi_{p,\lambda}^{\beta_1\gamma_1}(q) \bar{\chi}_{\lambda,p'}^{\beta_2\gamma_2*}(q) V_{p',k}^{\beta_2\beta} V_{k-q,p'-q}^{\alpha'\gamma_2} \quad (\text{S44})$$

of the quasi-particle, and $n_b(d_{2,\lambda}(q)) = 1/[\exp(d_{2,\lambda}(q)/T) - 1]$ is the Bose-Einstein distribution.

We get the Matsubara single-particle Green function with the first-order exciton correction

$$-\int d\tau e^{i\omega_k \tau} \langle T_{\tau} c_k(\tau) c_k^\dagger(0) \rangle = \frac{1}{i\omega_k - h^{\text{QAH}}(k) - \Sigma_k^{(H)}}, \quad (\text{S45})$$

In the quasi-particle picture, the single-particle Green function becomes

$$G_k(\omega_k) = -U_k^\dagger \langle c_k c_k^\dagger(\omega_k) \rangle U_k = \frac{1}{i\omega_k - d_k - \bar{\Sigma}_k^{(H)}} = \sum_s \frac{\bar{Z}_{k,s}}{i\omega_k - \bar{\epsilon}_{k,s}}, \quad (\text{S46})$$

where $\bar{\varepsilon}_{k,s}$ and $\bar{Z}_{k,s}$ are the poles and residues of $G_k(\omega_k)$, respectively, which satisfies sum rules $\sum_s \bar{Z}_{k,s} = I_2$ and $\sum_s \bar{Z}_{k,s} \bar{\varepsilon}_{k,s} = d_k$.

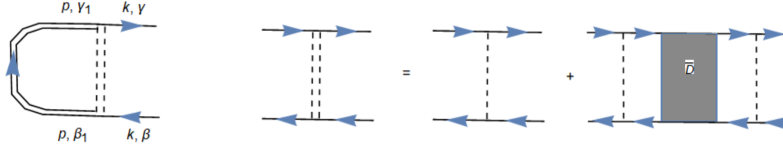


FIG. S15. The Fock-like self energy $\bar{\Sigma}_{k,\gamma\beta}^{(F)}$.

The Fock correction to the quasi-particle Green function can also be included as

$$\bar{\Sigma}_{k,\gamma\beta}^{(F)} = \sum_p T_{p,k}^{\beta_1\gamma_1,\beta\gamma}(q=0, \omega_q=0) T \sum_{\omega_p} \left[G_p^{\gamma_1\beta_1}(\omega_p) - \bar{G}_p^{(0)\gamma_1\beta_1}(\omega_p) \right], \quad (\text{S47})$$

where the interaction T -matrix is obtained by

$$T_{p,k}^{\beta_1\gamma_1,\beta\gamma}(q, \omega_q) = \mathcal{V}_{p,k}^{\beta_1\gamma_1,\beta\gamma} + \sum_{k'p'} \mathcal{V}_{p,k'}^{\beta_1\gamma_1,\mu_1\nu_1} \bar{D}_{k',p'}^{\mu_1\nu_1,\mu\nu}(q, \omega_q) \mathcal{V}_{p',k}^{\mu\nu,\beta\gamma}, \quad (\text{S48})$$

and

$$T \sum_{\omega_p} \left[G_p^{\gamma_1\beta_1}(\omega_p) - \bar{G}_p^{(0)\gamma_1\beta_1}(\omega_p) \right] = \sum_s \bar{Z}_{p,s}^{\gamma_1\beta_1} [f(\bar{\varepsilon}_{p,s}) - 1] + \delta_{\gamma_1\beta_1} (1 - f_k^{\gamma_1}) \quad (\text{S49})$$

is determined by $G_k(\omega_k)$ and $\bar{G}_p^{(0)\gamma_1\beta_1}(\omega_p) = \delta_{\gamma_1\beta_1}/(i\omega - d_{p,\gamma_1})$.

Finally, the full single-particle Green function including the Hartree-Fock-like corrections becomes

$$G_k^f(\omega_k) = \frac{1}{i\omega_k - d_k - \bar{\Sigma}_k^{(H)} - \bar{\Sigma}_k^{(F)}} = \sum_s \frac{Z_{k,s}}{i\omega_k - \varepsilon_{k,s}}, \quad (\text{S50})$$

where $\varepsilon_{k,s}$ and $Z_{k,s}$ are the poles and residues of the spectral function $G_k^f(\omega_k)$, respectively. The retarded Green's function $G_k^{(R)}(\omega) = G_k^f(i\omega_k \rightarrow \omega + i\eta)$ is obtained by the analytic continuation, which determines the spectral function $A_k(\omega) = -\text{Im}G_k^{(R)}(\omega)/\pi$. In our numerical calculation, we choose $\eta = 0.004$.

Due to the particle-hole symmetry, $A_k^v(x) = A_k^c(-x)$ and we only focus on the valence. Comparing with the spectral function of the free Green function $A_k^{(0)v}(x) = \delta(x - d_k^v)$, we find that when the temperature increases, not only the quasi-particle gap is reduced, but the broadened spectral function $A_k^v(x)$ even has the non-zero distribution at the positive frequency, as shown in Fig. S16. This is a strong evidence of the valence band electron dressed by the excitons. The reduction of the quasi-particle weight and the spectral distribution in the negative frequency domain indicates the decrease of the current-current correlation. As shown in Fig. 3, with the correction of the exciton the current-current correlation decreases much faster than the mean-field result. However, the perturbative expansion fails to predict the correct critical temperature obtained by XTRG. This is because at the higher temperature, many excitons are proliferated, which strongly affect the quasi-particle spectrum as well as the particle-hole spectrum. As a result, the bare Green function in the calculation of the T -matrix should be replaced by the exact Green function, namely, the self-consistent calculation of the Green function is required, which will be our future work.

In the CDW phase, the calculation on the T -matrix and self-energy corrections can also be performed in the similar way, which also shows the low lying exciton excitation confirmed by the XTRG results.

The Fourier transformation gives rise to the interacting Hamiltonian

$$H_I = \frac{1}{N} \sum_{k_h, \bar{k}_h, q_h} : c_{k_h - q_h, \alpha'}^\dagger \tilde{V}_{\alpha'\beta}^{k_h - q_h, k_{h+} - q_h; \bar{k}_h - q_h, \bar{k}_{h+} - q_h} c_{\bar{k}_h - q_h, \beta} c_{\bar{k}_h, \bar{\alpha}}^\dagger \tilde{V}_{\bar{\alpha}\beta'}^{\bar{k}_h, \bar{k}_{h+}; k_h, k_{h+}} c_{k_h, \beta'} : \\ + \frac{1}{N} \sum_{k_h, \bar{k}_h, q_h} : c_{k_h - q_h, \alpha'}^\dagger \tilde{V}_{\alpha'\beta}^{k_h - q_h, k_{h+} - q_h; \bar{k}_{h+} - q_h, \bar{k}_h - q_h} P_{\bar{\beta}\bar{\beta}'} c_{\bar{k}_h - q_h, \bar{\beta}'} c_{\bar{k}_h, \bar{\alpha}_1}^\dagger P_{\bar{\alpha}_1\bar{\alpha}} \tilde{V}_{\bar{\alpha}\beta'}^{\bar{k}_{h+}, \bar{k}_h; k_h, k_{h+}} c_{k_h, \beta'} : \quad (\text{S51})$$

in the momentum space $c_{k_h} = (a_{k_h}, b_{k_h}, a_{k_{h+}}, b_{k_{h+}})$, where the 4×4 interacting matrix $\tilde{V}^{k,k';p,p'} = \begin{pmatrix} V_k^\dagger M V_p & 0 \\ 0 & V_{k'}^\dagger M V_{p'} \end{pmatrix}$ and the permutation matrix $P = \sigma^x \otimes I_2$.

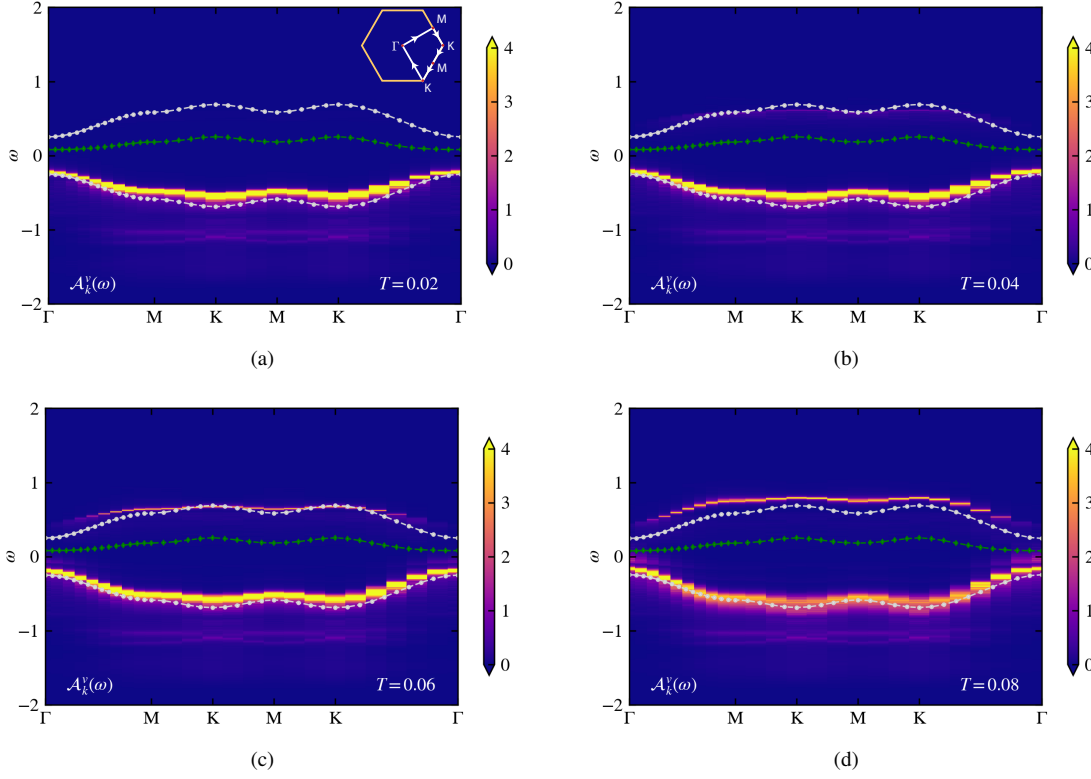


FIG. S16. The conductive and valence bands of the free single-particle Green's function (white dots), the exciton band (green diamonds), and the spectral function $A_k^v(\omega)$ of the full single-particle Green's function on the valence band at $T = 0.02, 0.04, 0.06$ and 0.08 for $\alpha = 0.2$ (QAH phase). As temperature increases, the proliferation of excitons manifests.

The two-particle spectrum is also obtained by the ladder diagram approximation. The self-energy correction, e.g., the Hartree term, becomes

$$\Sigma_{k_h, \alpha\beta}^{(\text{H})\text{CDW}} = - \left(\frac{2}{N} \right)^2 \sum_{p_h, p'_h, q_h} \frac{1}{\beta} \sum_{\omega_{q_h}} G_{k_h - q_h, \alpha_1 \alpha_2}^{(0)\text{CDW}}(\omega_{k_h} - \omega_{q_h}) D_{p_h p'_h}^{\beta_1 \gamma_1, \beta_2 \gamma_2}(q_h, \omega_{q_h}) \quad (\text{S52})$$

$$\left[\tilde{V}_{\alpha\beta_1}^{k_h, k_{h+}; p_h, p_{h+}} \tilde{V}_{\gamma_1 \alpha_1}^{p_h - q_h, p_{h+} - q_h; k_h - q_h, k_{h+} - q_h} + P_{\alpha\alpha'} \tilde{V}_{\alpha'\beta_1}^{k_{h+}, k_h; p_h, p_{h+}} \tilde{V}_{\gamma_1 \alpha_1}^{p_h - q_h, p_{h+} - q_h; k_{h+} - q_h, k_h - q_h} P_{\alpha_1 \alpha_1'} \right]$$

$$\left[\tilde{V}_{\beta_2 \beta}^{p_h, p_{h+}; k_h, k_{h+}} \tilde{V}_{\alpha_2 \gamma_2}^{k_h - q_h, k_{h+} - q_h; p_h - q_h, p_{h+} - q_h} + P_{\beta_2 \beta_2'} \tilde{V}_{\beta_2' \beta}^{p_{h+}, p_h; k_h, k_{h+}} \tilde{V}_{\alpha_2 \gamma_2'}^{k_h - q_h, k_{h+} - q_h; p_{h+} - q_h, p_h - q_h} P_{\gamma_2' \gamma_2} \right],$$

where the free single-particle Green function $G_{k_h}^{(0)\text{CDW}}(\omega_{k_h}) = 1/(i\omega_{k_h} - h^{\text{CDW}}(k_h))$. The exciton spectrum can be determined by the density-density correlation function

$$D_{p_h p'_h}^{\beta_1 \gamma_1, \beta_2 \gamma_2}(q_h, \omega_{q_h}) = \int_0^\beta d\tau D_{p_h p'_h}^{\beta_1 \gamma_1, \beta_2 \gamma_2}(q_h, \tau) e^{i\omega_{q_h} \tau}, \quad (\text{S53})$$

$$D_{p_h p'_h}^{\beta_1 \gamma_1, \beta_2 \gamma_2}(q_h, \tau) = - \langle T_\tau c_{p_h - q_h, \gamma_1}^\dagger(\tau) c_{p_h, \beta_1}(\tau) c_{p'_h, \beta_2}^\dagger(0) c_{p'_h - q_h, \gamma_2}(0) \rangle. \quad (\text{S54})$$

It follows from the Heisenberg EOM that

$$-\partial_\tau D_{p_h p'_h}^{\beta_1 \gamma_1, \beta_2 \gamma_2}(q_h, \tau) = \langle c_{p_h - q_h, \gamma_1}^\dagger c_{p_h - q_h, \gamma_2} \rangle G \delta_{\beta_1, \beta_2} - \langle c_{p_h, \beta_2}^\dagger c_{p_h, \beta_1} \rangle G \delta_{\gamma_1, \gamma_2} \delta_{\bar{p}_h, p_h} \delta(\tau) + M_{\bar{p}_h, k_h}^{\beta_1 \gamma_1, \beta_2 \gamma_2}(q_h) D_{k_h p_h}^{\beta_1 \gamma_1, \beta_2 \gamma_2}(q_h, \tau), \quad (\text{S55})$$

where

$$\begin{aligned}
M_{\bar{p}_h, \bar{k}_h}^{\beta_1 \gamma_1, \beta \gamma}(q_h) &= (h_{\beta_1 \beta}^{\text{CDW}}(\bar{p}_h) \delta_{\gamma_1 \gamma} - \delta_{\beta_1 \beta} h_{\gamma \gamma_1}^{\text{CDW}}(\bar{p}_h - q_h)) \delta_{\bar{p}_h, \bar{k}_h} \\
&+ \frac{2}{N} \left[\left(\tilde{V}_{\gamma \gamma_1}^{\bar{k}_h - q_h, \bar{k}_h + - q_h; \bar{p}_h - q_h, \bar{p}_h + - q_h} \tilde{V}_{\bar{\alpha} \beta}^{\bar{p}_h, \bar{p}_h +; \bar{k}_h, \bar{k}_h +} + \tilde{V}_{\gamma \beta_1}^{\bar{k}_h - q_h, \bar{k}_h + - q_h; \bar{p}_h + - q_h, \bar{p}_h - q_h} P_{\beta_1 \gamma_1} P_{\bar{\alpha} \alpha_1} \tilde{V}_{\bar{\alpha} \beta}^{\bar{p}_h +, \bar{p}_h; \bar{k}_h, \bar{k}_h +} \right) \langle c_{\bar{p}_h, \bar{\alpha}}^\dagger c_{\bar{p}_h, \beta_1} \rangle_G \right. \\
&\left. - \left(\tilde{V}_{\gamma \beta}^{\bar{k}_h - q_h, \bar{k}_h + - q_h; \bar{p}_h - q_h, \bar{p}_h + - q_h} \tilde{V}_{\beta_1 \beta}^{\bar{p}_h, \bar{p}_h +; \bar{k}_h, \bar{k}_h +} + \tilde{V}_{\gamma \beta_1}^{\bar{k}_h - q_h, \bar{k}_h + - q_h; \bar{p}_h + - q_h, \bar{p}_h - q_h} P_{\beta_1 \beta} P_{\beta_1 \bar{\alpha}_1} \tilde{V}_{\beta_1 \beta}^{\bar{p}_h +, \bar{p}_h; \bar{k}_h, \bar{k}_h +} \right) \langle c_{\bar{p}_h - q_h, \gamma_1}^\dagger c_{\bar{p}_h - q_h, \beta} \rangle_G \right].
\end{aligned} \tag{S56}$$

We define the correlation function $\bar{D}_{p'_h p_h}^{\beta_1 \gamma_1, \beta_2 \gamma_2}(q, \tau) \equiv D_{p'_h p_h}^{\beta_1 \gamma_1, \beta_2 \gamma_2}(q, \tau) U_{p'_h - q, \gamma_1 \gamma_1}^\dagger U_{p'_h, \beta_1 \beta_1}^\dagger U_{p_h, \beta_2 \beta_2} U_{p_h - q, \gamma_2 \gamma_2}^\dagger$ in the quasi-particle basis via the transformation U_{p_h} in the CDW phase. The Fourier transform of EOM (S55) results in

$$\bar{D}_{p'_h p_h}^{\beta_1 \gamma_1, \beta_2 \gamma_2}(q_h, \omega_{q_h}) = \left(\frac{1}{i\omega_{q_h} - \bar{M}(q_h)} \right)_{\bar{p}_h, \bar{k}_h}^{\beta_1 \gamma_1, \beta \gamma} \bar{N}_{\bar{k}_h p_h}^{\beta \gamma, \beta_2 \gamma_2}(q_h, \omega_{q_h}), \tag{S57}$$

$$\bar{M}_{\bar{p}_h, \bar{k}_h}^{\beta_1 \gamma_1, \beta \gamma}(q_h) = (d_{\bar{p}_h, \beta_1} \delta_{\gamma_1, \gamma} - \delta_{\beta_1, \beta} d_{\bar{p}_h - q_h, \gamma_1 \gamma}) \delta_{\bar{p}_h, \bar{k}_h} + \mathcal{V}_{\bar{p}_h, \bar{k}_h}^{(h, h_+) \beta_1 \gamma_1, \beta \gamma}(q_h) \left(f_{\bar{p}_h - q_h}^{\gamma_1} - f_{\bar{p}_h}^{\beta_1} \right), \tag{S58}$$

$$\bar{N}_{\bar{p}_h p_h}^{\beta_1 \gamma_1, \beta_2 \gamma_2}(q, \omega_q) = (f_{p_h - q}^{\gamma_1} - f_{p_h}^{\beta_1}) \delta_{p_h, \bar{p}_h} \delta_{\beta_1, \beta_2} \delta_{\gamma_1, \gamma_2}, \tag{S59}$$

where the interaction

$$\mathcal{V}_{\bar{p}_h, \bar{k}_h}^{(h, h_+) \beta_1 \gamma_1, \beta \gamma}(q_h) = \frac{2}{N} \left(-V_{\bar{k}_h - q_h, \bar{p}_h - q_h}^{(h, h_+) \gamma \gamma_1} V_{\bar{p}_h, \bar{k}_h}^{(h, h_+) \beta_1 \beta} - V_{\bar{k}_h - q_h, (P)\bar{p}_h - q_h}^{(h, h_+) \gamma \gamma_1} V_{(P)\bar{p}_h, \bar{k}_h}^{(h, h_+) \beta_1 \beta} \right) \tag{S60}$$

of two quasi-particles is determined by $V_{\bar{k}_h - q_h, \bar{k}_h}^{(h, h_+) \gamma \beta} \equiv U_{\bar{k}_h - q_h, \gamma \gamma'}^\dagger \tilde{V}_{\gamma' \beta'}^{\bar{k}_h - q_h, \bar{k}_h + - q_h; \bar{k}_h, \bar{k}_h +} U_{\bar{k}_h, \beta' \beta}$ and $V_{(P)\bar{p}_h, \bar{k}_h}^{(h, h_+) \beta_1 \beta} \equiv U_{\bar{p}_h, \beta_1 \gamma'}^\dagger P_{\gamma' \alpha_1} \tilde{V}_{\alpha_1 \beta'}^{\bar{p}_h +, \bar{p}_h; \bar{k}_h, \bar{k}_h +} U_{\bar{k}_h, \beta' \beta}$. The spectral decomposition results in

$$\bar{D}_{p'_h p_h}^{\beta_1 \gamma_1, \beta_2 \gamma_2}(q_h, \omega_{q_h}) = \chi_{\bar{p}_h, \lambda}^{\beta_1 \gamma_1}(q_h) \frac{1}{i\omega_{q_h} - d_{2, \lambda}(q_h)} \bar{X}_{p_h, \lambda}^{\beta \gamma *}(q_h). \tag{S61}$$

In the CDW phase, the lowest band with the dispersion relation $d_{\text{ex}}(q) = \min_\lambda |d_{2, \lambda}(q)|$ also corresponds to a collective mode, i.e., the exciton excitation. The lowest energy of the exciton is about 0.15 for $\alpha = 0.1$, which is smaller than the quasi-particle gap, similar to what happens in the QAH phase. However, the exciton band structure in the CDW phase is significantly distinct from that in the QAH phase due to the different spatial symmetries, as shown in Fig. S17.

The self-energy corrections, i.e., the Hartree-Fock corrections $\bar{\Sigma}_k^{(\text{H})\text{CDW}}$ and $\bar{\Sigma}_k^{(\text{F})\text{CDW}}$, can also be obtained in the similar way as Eq. (S44) and Eq. (S47). One only has to change the corresponding quasi-particle Green function and the interaction matrix to those in the CDW phase, which results in the full single-particle Green function

$$G_{k_h}^{\text{CDW}}(\omega_{k_h}) = -\langle c_{k_h} c_{k_h}^\dagger(\omega_{k_h}) \rangle = \frac{1}{i\omega_{k_h} - U_{k_h}^\dagger h_{k_h}^{\text{CDW}}(k_h) U_{k_h} - \bar{\Sigma}_{k_h}^{(\text{H})\text{CDW}} - \bar{\Sigma}_{k_h}^{(\text{F})\text{CDW}}} \tag{S62}$$

and the spectral functions $A_k^\beta(\omega)$. Due to the symmetries mentioned in the last section, there are two degenerate valence bands and two degenerate conductance bands, as a result, four single-particle spectral functions are obtained in the CDW phase. Due to the particle-hole symmetry, we only focus on the spectral function $A_k^v(\omega)$ for one of the degenerate valence bands. When the temperature increases, the quasi-particle gap is reduced and the exciton mode assists the valence electron to tunnel across the band gap, as shown in Fig. S18.

Via choosing the specific path in the momentum space, as illustrated in Fig. S19, the difference of the spectral function between the QAH and CDW phases are explicitly displayed. In our case, the period of the spectral function in the CDW phase is reduced by half in the y direction. In the QAH phase, the translational symmetry $P_{\vec{d}_i}$ ($i = 1, 2, 3$) are preserved. However, the stripe in the CDW phase spontaneously breaks the translational symmetry $P_{\vec{d}_i}$ ($i = 1, 2, 3$) and preserves the translational symmetry $P_{2\vec{d}_i}$ ($i = 1, 2, 3$), as a result, the period in the momentum space is reduced.

Section IX: Numerical results on Haldane-Hubbard model

We perform DMRG ($T = 0$) and XTRG ($T > 0$) calculations of the spinless Haldane-Hubbard model (HHM) whose Hamiltonian reads

$$H = -t \sum_{\langle ij \rangle} (c_i^\dagger c_j + \text{h.c.}) - t' \sum_{\langle\langle ij \rangle\rangle} (e^{i\phi_{ij}} c_i^\dagger c_j + \text{h.c.}) + V \sum_{\langle ij \rangle} (n_i - \frac{1}{2})(n_j - \frac{1}{2}), \tag{S63}$$

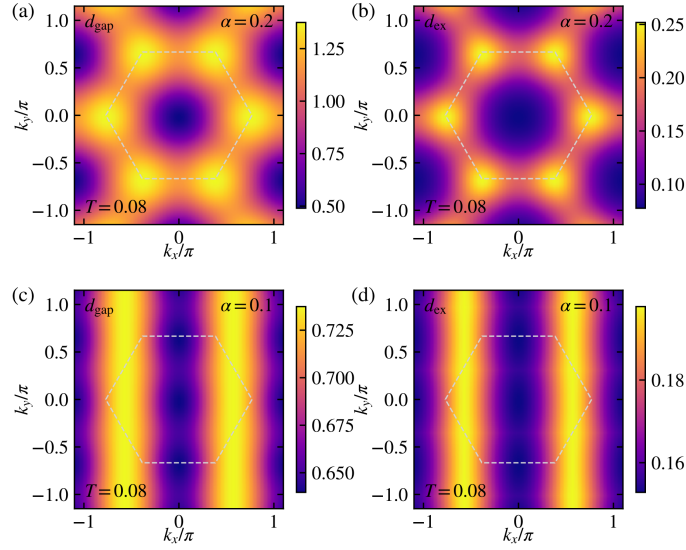


FIG. S17. The quasi-particle gap $d_{gap} = 2d_{k,c}(2E_k)$ and the exciton band d_{ex} in the QAH (CDW) phase, where $\alpha = 0.2(0.1)$. The exciton energy is one order of magnitude smaller than the quasi-particle gap. Besides, the bands in the CDW phase have the reduce period in the y direction.

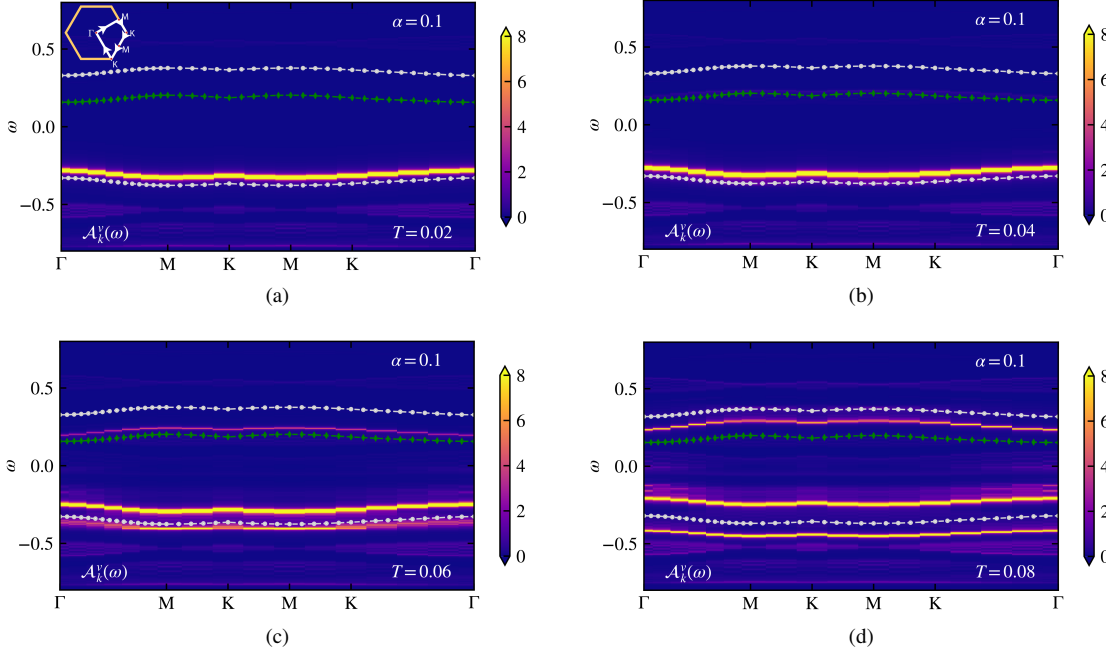


FIG. S18. The conductive and valence bands (white dots), the exciton band (green diamonds), and the spectral function $A_k^v(\omega)$ at $T = 0.02, 0.04, 0.06$ and 0.08 for $\alpha = 0.1$ in the CDW phase.

where $t' = 0.2t$, $\phi_{ij} = \frac{\pi}{2}$ and the direction of next-nearest-neighbor (NNN) pair $\langle\langle ij \rangle\rangle$ follows the standard Haldane model [84], and introduce the nearest-neighbor (NN) repulsion as in, e.g., Ref. [83]. The model in Eq. (S63) keeps the particle-hole symmetry and thus guarantees half filling in the finite-temperature XTRG calculations below. $t = 1$ is set as the energy scale below.

In Fig. S20(a), we show the DMRG results of charge density difference $(n_A - n_B) \equiv \frac{2}{N}(\sum_{i \in A} n_i - \sum_{i \in B} n_i)$ between sublattice A and B, which serves as an order parameter of the charge density wave (CDW) phase with large V . Around $V_c \simeq 2.01$, we find a sudden jump from zero to finite value in $n_A - n_B$, which suggests a first-order phase transition there. Note that, this transition V_c is half of the corresponding value in Ref. [83], due to the fact that, for the spinless fermion here, half of the Coulomb interaction terms (i.e. those $n_{i\uparrow}n_{j\downarrow}$ terms) are discarded.

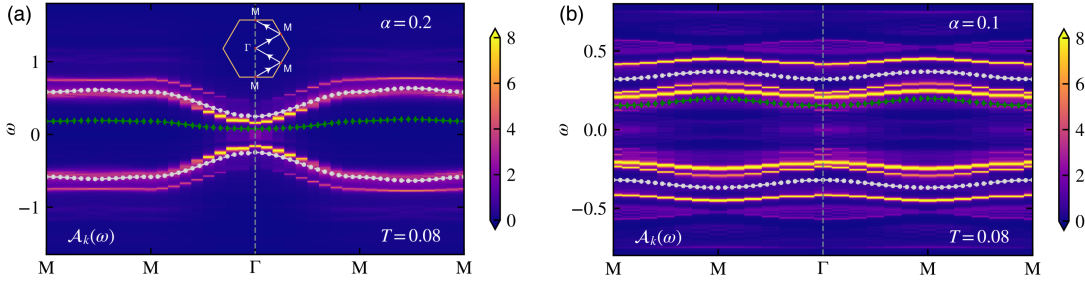


FIG. S19. The single-particle spectral function $\mathcal{A}_k(\omega) = \mathcal{A}_k^v(\omega) + \mathcal{A}_k^c(\omega)$ for both the valence and conductive bands. (a) $\alpha = 0.2$ (QAH phase) and (b) $\alpha = 0.1$ (CDW phase). The period of the spectral function in the CDW phase is reduced by half.

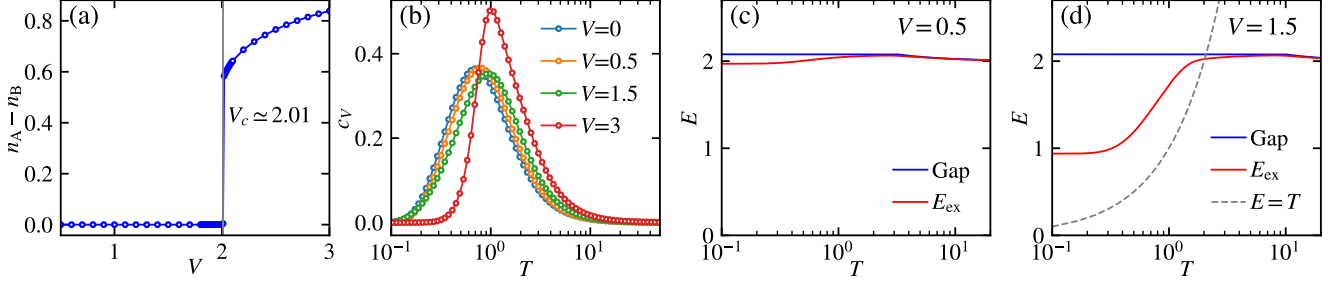


FIG. S20. In a $YC4 \times 12 \times 2$ Haldane-Hubbard model, (a) sub-lattice charge density difference $n_A - n_B$ obtained from DMRG calculation are shown versus nearest neighboring Coulomb repulsion strength V . (b) Specific heat c_V obtained from XTRG calculation is shown versus temperature T for different cases, i.e. $V = 0, 0.5, 1.5$ (CI) and $V = 3$ (CDW). (c,d) Band gap and exciton energy obtained from field-theoretical calculation are shown versus temperature T for $V = 0.5, 1.5$.

In Fig. S20(b) we present the XTRG results of the specific heat in the cases with $V = 0, 0.5, 1.5$ (CI) and $V = 3$ (CDW). As temperature rises up, in both phases, i.e., CDW and CI, the specific heat establishes round peaks (instead of divergent ones). Note that, with the increasing interaction strength from $V = 0$ to $V = 1.5$ in the CI phase, the position of the specific heat round peaks moves to higher temperatures. It contradicts the exciton proliferation picture, where the larger binding energy induced by interactions (the extremely lower exciton excitation mode) gives rise to the lower position of the specific round peaks as V increases.

As shown in Fig. S20(c-d), the fluctuation spectra analysis confirms that the exciton bounded states are hardly occupied in the CI phase of the HHM, in stark contrast to the TBG model where exciton proliferation occurs in the QAH phase. The reason why excitons are rarely occupied in the HHM is that the exciton energy scale is always higher than the system temperature. Here are two cases: (a) When the nearest-neighbor interaction V is relatively small (say, $V = 0.5$), as illustrated in Fig. S20(c), the Haldane term predominates and the exciton energy remains roughly at the same value of the energy gap 2 even if the temperature increases. (b) It is even more interesting for a larger V (say, $V = 1.5$). As temperature increases, the attractive interaction between electrons and holes is screened by the individual thermal excitations, resulting in a reduced exciton binding energy and a larger spatial distribution of the exciton wavefunction. For instance, the exciton energies are $E_{ex} \simeq 0.8, 1.1$, and 1.7 for $V = 1.5$ at temperatures $T = 0, 0.5$ and 1, respectively. As shown in Fig. S20(d), the exciton energy is always higher than the corresponding temperature, therefore the exciton modes are hardly populated by thermal fluctuations. This explains why the specific heat curves in Fig. S20(b) change only slightly as V increases from 0 to 1.5.

With the above numerical calculations and field-theoretical analysis on HHM, we conclude a fundamental difference in terms of distinct exciton energies and thermal properties when compared to the flat-band twisted bilayer graphene systems. The uniqueness of the latter originates from the interaction-driven, emergent, single-particle band in the strongly coupling limit.